

Three-band Anderson-Mott-Hubbard model for the metal-insulator transition in cubic disordered tungsten bronzes Na_xWO_3 and $\text{Na}_x\text{Ta}_y\text{W}_{1-y}\text{O}_3$

Hartmut Dücker and Wolfgang von Niessen

Institut für Physikalische und Theoretische Chemie, Hans-Sommer-Strasse 10, D-38106 Braunschweig, Germany

Thorsten Koslowski

Institut für Physikalische Chemie und Elektrochemie I, Universität Karlsruhe, Kaiserstraße 12, D-76128 Karlsruhe, Germany

Michael A. Tusch and David E. Logan

Physical and Theoretical Chemistry Laboratory, University of Oxford, South Parks Road, Oxford, OX1 3QZ, United Kingdom

(Received 8 December 1997)

A microscopic three-band Anderson-Mott-Hubbard model for cubic disordered tungsten bronzes Na_xWO_3 and $\text{Na}_x\text{Ta}_y\text{W}_{1-y}\text{O}_3$ is studied over a range of doping levels $x-y$ at the level of an unrestricted Hartree-Fock approximation in order to understand the effects of disorder and electron interaction on the electronic ground state and their implications for the chemically induced metal-insulator transition observed at least in the latter materials. For sufficiently large U a pseudogap develops at E_F in agreement with photoemission spectra and tunneling current measurements which is found to significantly affect the localization and hybridization characteristics as well as the three-dimensional spatial distribution of quasiparticle states and thus constitutes the central feature of the model. The formation of the pseudogap is rationalized via a repulsion between occupied and unoccupied conduction band quasiparticle states induced by antiferromagnetic correlations occurring on length scales which—for the most relevant parameters—are controlled by the doping-dependent tight-binding Fermi surface. Light is shed on experimental results which hitherto have not found a satisfactory rationalization. [S0163-1829(99)04802-X]

I. INTRODUCTION

A detailed understanding of the factors which influence a metal-insulator transition (MIT) driven by the progressive filling of a conduction band (CB) in a solid—in practice achieved by varying its chemical composition and thus disorder—is a continuing problem that has challenged both experimentalists and theorists for many years.¹ The simplest theoretical example of such occurs in a disordered but non-interacting model such as the single-band Anderson model, in which disorder leads to localization of single-particle states at the band edges.^{2,3} The system then displays a MIT as the Fermi level crosses the mobility edge separating regimes of localized and extended states. In real systems, however, electron interactions frequently occur on an energy scale similar to the bandwidth and disorder strength, leading to rather complex behavior which has proved notoriously difficult to describe.¹ This is particularly evident in the intensively studied case of transition metal oxides, in which the dominant interactions occur between electrons in the d orbitals of a given transition metal site. Of these, perovskites form a large and important class, whose relatively simple crystal structure (Fig. 1) renders them particularly amenable to both experimental and theoretical investigation, and which has received much recent attention due to the discovery of high- T_c superconductivity in closely related cuprate compounds. The chemical composition of perovskites of formula ABO_3 may be precisely varied and controlled—either by substitution or removal of the electropositive element A or by substitution of the transition metal B —enabling a MIT to be induced and studied in considerable detail.^{4,5} These materials

are known as bronzes, after the original and most highly studied example of sodium tungsten bronze Na_xWO_3 (discovered in 1823 by Wöhler⁶), on which we here focus. For reviews on structural and electronic properties of tungsten bronzes see Refs. 7, 8, and 9; additionally some theoretical aspects have been discussed by Mott.¹⁰

Undoped WO_3 is a charge-transfer insulator of band gap 3 eV. Overlap between O $2s$, O $2p$, and W $5d$ orbitals gives rise to filled valence (bonding) bands (VB's), associated predominantly with O and empty conduction bands (antibonding) of mainly W character.¹¹

Numerous experiments^{9,12} and band structure calculations¹³⁻¹⁷ imply that the Na atoms are ionized, their valence electrons entering the $t_{2g}(\pi^*)$ conduction band of WO_3 . By chemically controlling the sodium content x , the CB filling fraction can be continuously varied between zero and 1/6, corresponding to the perovskite NaWO_3 in which all interstitial sites are occupied. Fully doped NaWO_3 , which

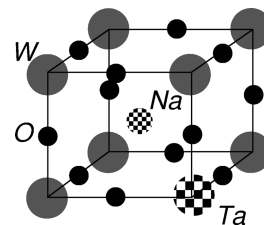


FIG. 1. Cubic unit cell of perovskites ABO_3 . The transition metal atoms B and oxygens are located at the corners and edges of the cube, respectively. The electropositive element A occupies the interstitial.

closely resembles ReO_3 , has roughly the conductivity (σ) of copper.⁹ As x is decreased from unity—and the CB filling fraction correspondingly lowered from $1/6$ —the sign of $d\sigma/dT$ changes at $x \approx 0.3$,¹⁸ but the system remains metallic down to $x \approx 0.21$.¹⁹ At this composition the system is believed to be close to a MIT, mainly attributed to Anderson localization¹⁰ resulting from Coulombic disorder generated by the randomly disposed Na^+ ions, although a generalized Mott criterion for a correlation-induced MIT has also been found to be applicable to this system.²⁰ Direct examination of the MIT is difficult, however, since below $x \approx 0.4$ the cubic phase (which itself exhibits slight distortions²¹) is metastable, a two-phase mixture of tetragonal and cubic structures being the stable form down to $x \approx 0.28$,²² below which a tetragonal phase²³ or a mixture of various phases²² results. Recently, cubic samples with x as low as 0.14 have been found to be superconducting²⁴ but no information on the normal state properties has been given. However, at low doping the tetragonal phase is reported to be insulating²⁵ (and we note that the MIT is not believed to be driven by the structural phase transition¹⁰). Investigation of the MIT stems from experiments on Ta-substituted bronzes $\text{Na}_x\text{Ta}_y\text{W}_{1-y}\text{O}_3$, in which the structural phase transition can be suppressed.²⁶ In these systems, the doping level is $x-y$ since Ta has one fewer electron than W. The electronic properties of these materials are similar to the unsubstituted compounds at the same doping level—for example, $d\sigma/dT$ is also found to change sign at $x-y \approx 0.3$ (Ref. 27)—but their conductivities are systematically reduced; this has been attributed to the additional disorder created by the Ta impurities.¹⁸ From the limiting behavior of the conductivity at low T the MIT has been positioned at $x-y$ between 0.18 and 0.19.^{18,28}

Recent experiments have provided clear evidence that a purely disorder-induced Anderson transition cannot fully account for the nature of the MIT. For example, Raychaudhuri has concluded from detailed low- T studies that strong interaction effects express themselves in the temperature dependence of the conductivity $d\sigma/dT$ in both metallic and insulating regimes.¹⁸ Most significantly, direct evidence for the importance of electron interactions has been obtained from tunneling current measurements^{29,30} and photoemission studies:^{31–33} these clearly reveal the existence of a pseudogap at the Fermi level E_F over a range of doping levels within the metallic phase, which may even develop into a soft gap within the insulator. The existence of a pseudogap is further consistent with the observation of a Friedman anomaly in the T dependence of the Hall coefficient, i.e., a freezing out of charge carriers at low T [at least for $x = 0.22$ (Ref. 19)], although several alternative scenarios have been proposed^{10,34}—see Sec. III for a discussion.

Well within the metallic phase the pseudogap, which occurs on a scale of ≈ 50 – 100 meV, is found to have square-root edges, consistent with the well-known prediction from Fermi liquid theory for a three-dimensional (3D) disordered, interacting electron system, that the spectral density $D(E) \propto |E - E_F|^{1/2}$ near E_F .³⁵ As the MIT is approached from the metallic side, the pseudogap edges become distinctly linear, which has been interpreted as a breakdown of Fermi liquid theory within the metal.²⁹ In the insulator the classical Coulomb gap model³⁶ has been invoked to explain the possible existence of a soft gap. Further indication of the

importance of strong interactions is provided by NMR (Refs. 37–39) and electron spin resonance²⁵ (ESR) studies, to which we will refer in Sec. VI.

Tungsten bronzes thus clearly exhibit the properties of a multiband system arising from overlap of s , p , and d orbitals on different species together with the effects of strong electron interactions, and varying disorder generated by the dopant Na or substituent Ta atoms.

To gain a deeper understanding of the origins of these properties we investigate an electronic model which we believe faithfully incorporates the principal effects of these factors. To motivate our choice of model Hamiltonian we first note that a variety of experimental probes—including inelastic neutron scattering,⁴⁰ positron annihilation,⁴¹ and constant initial state (CIS) photoemission⁴²—of the Fermi surface over a range of doping levels well within the metallic phase of Na_xWO_3 demonstrate that a tight-binding (TB) model including only nearest-neighbor (NN) hopping⁴³ gives a good description of the underlying band structure. Such a rigid band model cannot, of course, describe the insulator or the approach to the MIT from the metallic side. We therefore incorporate into the TB Hamiltonian both disorder and electron interactions as follows. We model the disorder generated by the Coulomb fields of the randomly disposed Na^+ ions via microscopically correlated disorder in the W and O site energies. The primary effects of electron interactions are represented via an on-site Hubbard U for W $5d$ orbitals; in passing we note that a purely on-site repulsion is likely to be most realistic in the metallic phase due to screening of the long-ranged Coulomb interaction by itinerant electrons.

With the resultant multiband Anderson-Mott-Hubbard (AMH) model we seek to address the following questions.

Under what conditions will a pseudogap arise in the single-particle spectrum in both metallic and insulating phases, what is its microscopic origin, and how can its occurrence be reconciled with the existence of a well-defined Fermi surface well into the metallic regime?

What are the localization characteristics of single-particle excitations, particularly in the vicinity of the Fermi level, and how do the combined effects of disorder and electron-electron interactions influence the MIT?

What are the implications of the formation of a pseudogap on the nature of the chemical bonding as the doping level is varied?

What are the principal effects of Ta substitution?

The model Hamiltonian represents an interacting many-body problem with the statistical complexities of a disordered system. We require an approximation that is qualitatively applicable both to the metallic and insulating phases, and is able to account for the broad features of the MIT.

Analytical methods such as disordered Fermi liquid theory, while powerful well into the metallic phase, break down as the MIT is approached and are, of course, inapplicable in the insulating regime. Numerical methods such as exact diagonalization and quantum Monte Carlo are limited to very small system sizes—far too small to infer any information on localization properties or the MIT. We here adopt an unrestricted Hartree-Fock (UHF) approximation for the following reasons: (i) It is capable of describing, at least qualitatively, both the metallic and insulating phases. (ii) The UHF approach represents the simplest nontrivial approxima-

tion which can account for the first effects of strong interactions in leading to local moment formation. (iii) Disorder can be treated exactly, subject to averaging over finite-sized systems. (iv) Efficient numerical algorithms allow large systems to be studied, enabling the pseudogap and localization properties to be reasonably resolved and the corresponding MIT to be identified.

Point (ii) perhaps requires further clarification in the present context. A mean-field approximation such as UHF predicts that, when local moments exist, they occur on arbitrarily long time scales (whether characterized by some \mathbf{q} vector or spin glasslike). Such magnetic “ordering” does not occur experimentally in tungsten bronzes. Nonetheless, in providing a snapshot of the correlations in a fluctuating local moment system, the UHF approximation permits a good qualitative interpretation of the effect of such correlations on the electronic structure—a central theme of this study.

The outline of the article is as follows. In Sec. II we derive the model, describe its treatment within UHF, and outline the assessment of localization properties. Section III presents detailed results for the Na_xWO_3 system, focusing on the density, localization, and spatial distribution of single-particle states. In Sec. IV we rationalize the emergence of the pseudogap microscopically in terms of the effects of interactions in leading to magnetic correlations within a system of disordered itinerant electrons. We examine the effect of the additional disorder introduced by Ta substitution in Sec. V, followed by concluding remarks in Sec. VI.

II. MODEL

To derive a tractable model Hamiltonian, we take advantage of an underlying symmetry of the cubic WO_3 host band structure which emerges within a tight-binding description. First, we note that the cubic crystal field splits the conduction bands into $t_{2g}(\pi^*)$ and $e_g(\sigma^*)$ manifolds, of which the former, arising from planar W $5d(t_{2g})$ and O $2p(\pi)$ overlap, lies lower in energy. Bands derived from the sodium valence orbitals are found to lie 11 eV above the Fermi level:¹² as mentioned in Sec. I, Na valence electrons enter the WO_3 CB. As shown originally by Wolfram,⁴³ an excellent representation of the t_{2g} band structure is obtained by retaining only NN W-O hopping matrix elements. This observation has the following important consequences. First, a Hamiltonian describing the π bonding between W(t_{2g}) and O $2p$ orbitals can be rigorously decoupled from the full 17-band model. Second, since now only t_{2g} and $p(\pi)$ orbitals lying in a common plane are coupled, the t_{2g} CB states become fully two dimensional. Since the energy of a given single-particle CB state may now be specified by two components of the crystal momentum, the Fermi surface of the full 3D system is expected to show strong 2D characteristics. This is confirmed by the observation of a strong Kohn anomaly in phonon dispersion curves deep in the metallic phase.^{40,44} Furthermore, the topology and doping dependence of the Fermi surface of the full 3D system (again well into the metallic regime), as revealed by phonon spectra, CIS photoemission spectra,⁴² and positron annihilation studies,⁴¹ can be well described in terms of an effective 2D rigid band model.⁴⁵

Therefore cubic tungsten bronzes, while fully isotropic,

are expected to have electronic properties showing strong signatures of the underlying 2D nature of the π bonding—a feature which will remain on the inclusion of disorder and electron interactions. In practical terms, we may take full advantage of the above decoupling to study a three-band, one-orbital-per-site model in 2D, enabling the consideration of sufficiently large length scales to ascertain localization properties and investigate the detailed band structure. This is essential, since a previous study which ignored this aspect suffered from severe finite-size effects.⁴⁶ In Sec. III we consider the effects of incorporating beyond-NN transfer matrix elements, leading to a fully 3D system.

Disorder—arising from the random disposition of sodium ions—is accounted for microscopically by representing each sodium ion at interstitial site j by an attractive model potential which lowers the orbital energies at oxygen and transition metal sites i by $V(|\mathbf{r}^i - \mathbf{r}^j|)$. Electron interactions are incorporated via a Hubbard U on the d orbitals. The resultant three-band Anderson-Mott-Hubbard Hamiltonian is thus given by

$$\begin{aligned} \hat{H} &= \sum_{i,\sigma} \epsilon_i^0 \hat{n}_{i\sigma} + \sum_{\langle ij \rangle, \sigma} t_{ij} \hat{c}_{i\sigma}^\dagger \hat{c}_{j\sigma} \\ &+ \sum_{i,\sigma} V_{C;i} \hat{n}_{i\sigma} + \frac{1}{2} \sum_{i \in \text{W,Ta}; \sigma} U \hat{n}_{i\sigma} \hat{n}_{i-\sigma} \quad (1) \\ &= \hat{H}^{\text{TB}} + \hat{H}^{\text{dis}} + \hat{H}^{\text{int}}, \quad (2) \end{aligned}$$

where $\hat{c}_{i\sigma}^\dagger$ and $\hat{c}_{j\sigma}$ are fermion creation and annihilation operators, respectively, $\hat{n}_{i\sigma} \equiv \hat{c}_{i\sigma}^\dagger \hat{c}_{i\sigma}$, and $\langle \rangle$ denotes a sum over NN's only. The TB parameters $\epsilon_i^0 \in \{\epsilon_{\text{W},5d}, \epsilon_{\text{Ta},5d}, \epsilon_{\text{O},2p}\}$ and t_{ij} are derived from Harrison⁴⁷ using a fixed lattice spacing a of 3.78 Å and $V_{C;i} \equiv \sum_j^{\text{Na}} V(|\mathbf{r}^i - \mathbf{r}^j|)$. We note that, except for disorder, the Hamiltonian (1) is topologically equivalent to a simplified Emery model^{48–50} used in the context of high- T_c superconductors. However, in tungsten bronzes Na_xWO_3 the maximum CB filling fraction $x' (=x/6)$ is 1/6—i.e., far away from half-filling—due to the threefold degeneracy of the t_{2g} bands. For $V(|\mathbf{r} - \mathbf{r}^j|)$, either a cutoff potential (as proposed by Dasgupta and Halley for high- T_c systems⁵¹), which supplies a constant shift V_C per sodium ion to the orbital energies of the NN oxygen and tungsten sites, or a screened Coulomb potential has been employed. Most of the work has been done for $V_C = -0.3$ eV—which value corresponds roughly to the binding energy to a Coulombic donor in WO_3 (Ref. 10)—and compared to results of supplementary calculations for $V_C = -0.2$ and -0.1 eV, together with a Yukawa potential with screening radius $1/\lambda = 2.5$ Å and background dielectric constant $\epsilon_\infty = 5.3$.¹² We have considered values of U in the range 0–10 eV, which should be compared with a CB TB bandwidth of $\approx 2t$ where $t = 1.6$ eV is the modulus of the NN W-O transfer integral.

At this point it is instructive to diagonalize the nondisordered, tight-binding Hamiltonian \hat{H}^{TB} , which elucidates the nature of the underlying band structure, makes contact with the well-known Emery model,⁴⁸ and will form a starting point for our analysis of the pseudogap in Sec. IV.

Making the first canonical transformation, defined by

$$|\psi_{\mathbf{k}\sigma}^{(l)}\rangle = \frac{1}{\sqrt{N}} \sum_m e^{i\mathbf{k}\cdot\mathbf{r}_m} |\varphi_{m\sigma}^{(l)}\rangle, \quad (3)$$

where $|\varphi_{m\sigma}^{(l)}\rangle$ denotes an atomic spin orbital centered on site m , with $l \in \{1 \equiv W, 2 \equiv O^{(1)}, 3 \equiv O^{(2)}\}$, the TB Hamiltonian is rendered block diagonal:

$$\hat{H}_{\text{TB}} = \sum_{\mathbf{k}\sigma} \hat{H}_{\mathbf{k}\sigma}. \quad (4)$$

$\hat{H}_{\mathbf{k}\sigma}$ has matrix representation

$$\hat{H}_{\mathbf{k}\sigma} = \begin{pmatrix} \epsilon_{W,5d} & -i2t\gamma_{k_x} & -i2t\gamma_{k_y} \\ i2t\gamma_{k_x} & \epsilon_{O,2p} & 0 \\ i2t\gamma_{k_y} & 0 & \epsilon_{O,2p} \end{pmatrix} \quad (5)$$

in the subset $\{|\psi_{\mathbf{k}\sigma}^{(l)}\rangle, l \in \{1,2,3\}\}$, and $t \equiv |t_{ij}|$, $\gamma_{k_\alpha} \equiv \sin(\frac{1}{2}k_\alpha a)$. \hat{H}_{TB} can be simplified further by a second unitary transformation, $\hat{U}^\dagger \hat{H}_{\text{TB}} \hat{U}$. \hat{U} is block diagonal,

$$\hat{U} = \sum_{\mathbf{k}\sigma} \hat{U}_{\mathbf{k}\sigma}, \quad (6)$$

and the matrix representation of $\hat{U}_{\mathbf{k}\sigma}$ in the subset $|\psi_{\mathbf{k}\sigma}^{(l)}\rangle, l \in \{1,2,3\}$, is given by

$$\hat{U}_{\mathbf{k}\sigma} = \begin{pmatrix} 1 & 0 & 0 \\ 0 & \frac{i\gamma_{k_x}}{\sqrt{\gamma_{k_x}^2 + \gamma_{k_y}^2}} & \frac{\gamma_{k_y}}{\sqrt{\gamma_{k_x}^2 + \gamma_{k_y}^2}} \\ 0 & \frac{i\gamma_{k_y}}{\sqrt{\gamma_{k_x}^2 + \gamma_{k_y}^2}} & \frac{-\gamma_{k_x}}{\sqrt{\gamma_{k_x}^2 + \gamma_{k_y}^2}} \end{pmatrix}, \quad (7)$$

the columns of which define a new basis

$$\{\phi_{\mathbf{k}\sigma}^{(W)}, \phi_{\mathbf{k}\sigma}^{(1)}, \phi_{\mathbf{k}\sigma}^{(2)}\}. \quad (8)$$

Application to \hat{H}_{TB} yields

$$\hat{U}^\dagger \hat{H}_{\text{TB}} \hat{U} = \sum_{\mathbf{k}\sigma} \hat{U}_{\mathbf{k}\sigma}^\dagger \hat{H}_{\mathbf{k}\sigma} \hat{U}_{\mathbf{k}\sigma} \equiv \sum_{\mathbf{k}\sigma} \hat{H}_{\mathbf{k}\sigma}^\diamond, \quad (9)$$

where

$$\hat{H}_{\mathbf{k}\sigma}^\diamond = \begin{pmatrix} \epsilon_{W,5d} & -t(\mathbf{k}) & 0 \\ -t(\mathbf{k}) & \epsilon_{O,2p} & 0 \\ 0 & 0 & \epsilon_{O,2p} \end{pmatrix}. \quad (10)$$

The transformation (9) has thus decoupled a flat, nonbonding band

$$E_{\mathbf{k}\sigma}^{\text{nb}} = \epsilon_{O,2p} \quad (11)$$

at the unperturbed O $2p$ site energy from \hat{H}_{TB} , and from Eq. (10) π bonding and antibonding bands with energies

$$E_{\mathbf{k}\sigma}^{+,-} = \frac{1}{2}(\epsilon_{W,5d} + \epsilon_{O,2p}) \pm \sqrt{\frac{1}{4}\Delta^2 + t(\mathbf{k})^2} \quad (12)$$

result from a set of N independent two-level systems, with atomic limit (i.e., $t=0$) charge transfer gap $\Delta = \epsilon_{W,5d} - \epsilon_{O,2p}$ and a canonical transfer matrix element $t(\mathbf{k}) \equiv 2t\sqrt{\gamma_{k_x}^2 + \gamma_{k_y}^2}$.

From Eqs. (5)–(12) it is clear that the TB Hamiltonian employed here is formally equivalent to that of the three-band Emery model for CuO_2 planes in high- T_c systems with NN hopping only,⁴⁹ which reflects the topological equivalence of the π bonding in the WO_2 planes and the σ bonding between Cu $3d_{x^2-y^2}$ and O $2p(\sigma)$ orbitals. To our knowledge the second unitary transformation [Eq. (9)] was first used in the context of a simplified Emery model,⁶⁵ and in that case the site energies and Hubbard U are taken to be such that the O $2p$ bands fall in between lower and upper Hubbard bands of predominant Cu $3d$ character;^{49,50} holes doped into the CuO_2 planes thus enter the O $2p$ bands.

Note [from Eq. (12)] that the bandwidth B of the conduction and valence bands depends both on t and Δ :

$$B = \sqrt{\frac{1}{4}\Delta^2 + 8t^2} - \sqrt{\frac{1}{4}\Delta^2}. \quad (13)$$

Clearly $B \rightarrow 0$ in the limit $\Delta/t \rightarrow \infty$.

The Hamiltonian (1) is solved via a UHF approach. For conceptual and numerical convenience the resultant local moments are constrained to lie along a common z axis (“Ising-spin” UHF) with $S_z^{\text{tot}}=0$; we do not expect the restriction to collinear moments to have a significant effect on single-particle properties.⁵²

The UHF Hamiltonian corresponding to Eq. (1) is given by

$$\hat{H} = \sum_{\sigma} \hat{H}_{\sigma},$$

$$\hat{H}_{\sigma} = \sum_i \epsilon_i \hat{n}_{i\sigma} + \sum_{\langle ij \rangle} t_{ij} \hat{c}_{i\sigma}^\dagger \hat{c}_{j\sigma} + \sum_{i \in W, \text{Ta}} U \hat{n}_{i\sigma} \bar{n}_{i-\sigma}, \quad (14)$$

where the overbar denotes an expectation value over the UHF ground state, and the bare site energy $\epsilon_i \equiv \epsilon_i^0 + V_{C,i}$ has been defined. Equations (14) are solved self-consistently, in lattices with 2700–30 000 sites. During the iteration, only CB states are taken into account in the evaluation of the $\bar{n}_{i\sigma}$, since the valence band is filled and separated from the CB by a gap of about 2 eV. The diagonalization at each step is performed via the Lanczos^{53–56} algorithm and the total density of states (DOS) in the CB is calculated using the spectrum slicing method.^{57,58} Typically 15–20 iterations are required to ensure convergence, which is enforced with respect to both spin densities and the ground state energy. For the smallest system sizes at least 25 disorder realizations are taken into account in the evaluation of densities of states and the assessment of localization properties.

Local charges and magnetic moments follow from the converged eigenvector coefficients via

$$n_i = \sum_{\sigma} \bar{n}_{i\sigma} = \sum_{\alpha < F; \sigma} |a_{i\alpha\sigma}|^2, \quad (15)$$

$$\mu_i = \sum_{\sigma} \sigma \bar{n}_{i\sigma} = \sum_{\alpha < F; \sigma} \sigma |a_{i\alpha\sigma}|^2, \quad (16)$$

where $a_{i\alpha\sigma}$ is the eigenvector coefficient for the UHF CB state $|\alpha\sigma\rangle$. From Eq. (14), with effective σ -spin site energies for transition metal sites defined via $\epsilon_{i\sigma} \equiv \epsilon_i + U\bar{n}_{i-\sigma}$, i.e.,

$$\epsilon_{i\sigma} = \epsilon_i + \frac{1}{2}U(n_i - \sigma\mu_i), \quad (17)$$

it is clear that the self-consistent UHF Hamiltonian is formally equivalent to a disordered tight-binding Hamiltonian with correlated site-diagonal disorder (and additional off-diagonal disorder for the Ta-substituted case considered in Sec. V).

It is also helpful for later purposes to define the weight of single-particle states $|\alpha\sigma\rangle$ on tungsten and oxygen sites, via

$$q_{\alpha\sigma}^W \equiv \sum_{i \in W} |a_{i\alpha\sigma}|^2 = 1 - \sum_{i \in O} |a_{i\alpha\sigma}|^2 \equiv 1 - q_{\alpha\sigma}^O \quad (18)$$

in the basis of atomic spin orbitals. For (anti)bonding TB states, i.e., $E_{\alpha\sigma} = E_{\mathbf{k}\sigma}^{+,-}$, the tungsten population is given by⁶⁶

$$q_{\mathbf{k}\sigma}^{W+,-} = 1 - \frac{E_{\mathbf{k}\sigma}^{+,-} - \epsilon_{W,5d}}{2E_{\mathbf{k}\sigma}^{+,-} - \epsilon_{W,5d} - \epsilon_{O,2p}}. \quad (19)$$

TB states at the bottom of the CB, where $E_{\mathbf{k}\sigma}^+ = \epsilon_{W,5d}$ [see Eq. (12)], thus have pure nonbonding character, i.e., $q_{\mathbf{k}\sigma}^{W+} = 1$.

The localization characteristics of quasiparticle states are obtained from the system-size scaling behavior of the renormalized correlation length⁵⁹

$$\mathcal{L}_{\alpha\sigma}^{(n)} = \frac{\Lambda_{\alpha\sigma}^{(n)}}{\Lambda_{\text{Bloch}}^{(n)}}, \quad (20)$$

where

$$\Lambda_{\alpha\sigma}^{(n)} = \left(\frac{\sum'_{i,j} |a_{i\alpha\sigma}|^2 |a_{j\alpha\sigma}|^2 r_{ij}^n}{(q_{\alpha\sigma}^W)^2} \right)^{1/n}. \quad (21)$$

$\mathcal{L}_{\text{Bloch}}^{(n)}$ is the corresponding correlation length for Bloch states in the system of the same size, the prime denotes a sum over W (and Ta) sites only, and the exponent n is 1 or 2.⁵⁹ The minimum image convention⁶⁰ is used in connection with cyclic boundary conditions in the evaluation of r_{ij} . While $\Lambda_{\text{Bloch}}^{(1)}$ must be calculated numerically, it is readily shown that

$$\Lambda_{\text{Bloch}}^{(2)} = a \sqrt{\frac{L^2 + 2}{6}}, \quad (22)$$

where L is the linear system size in units of a . Here $\mathcal{L}_{\alpha\sigma}^{(n)}$ is in practice averaged over spin indices, a suitably small energy interval, and disorder realizations. Since the localization characteristics obtained from the system-size scaling behavior of $\mathcal{L}_{\alpha\sigma}^{(n)}$ are found to be independent of n in agreement

with the results of Ref. 59, $\mathcal{L}_{\alpha\sigma}^{(1)}$ and $\mathcal{L}_{\alpha\sigma}^{(2)}$ are used interchangeably throughout the paper. As a complementary measure of localization we additionally employ the participation ratio,⁶¹ defined here as

$$P_{\alpha\sigma} = \left(\frac{\sum'_{i,j} |a_{i\alpha\sigma}|^4}{(q_{\alpha\sigma}^W)^2} \right)^{-1}. \quad (23)$$

III. Na_xWO₃

In this section numerical results of the 2D model for Na_xWO₃ are discussed, i.e., density and localization characteristics of CB single-particle states, followed by an extension to 3D with an emphasis on localization properties.

Starting from the 2D TB Hamiltonian we first consider briefly the noninteracting ($U=0$) Anderson limit, where the randomly dispersed Na ions induce Coulombic disorder in the tungsten and oxygen bare site energies. The disorder is naturally greatest for $x=0.5$ where the corresponding site energy distributions are found to be Gaussian, becoming skewed to high (low) site energies at smaller (larger) filling fractions x' . Despite the attractive, short-ranged, and microscopically correlated nature of the effective potentials, no gap or pseudogap arises in the resultant CB DOS for any x ; i.e., no impurity band is split from the CB: the effects of disorder on the DOS are simply to broaden the band and to round the van Hove singularities.

On introducing the Hubbard U the effective σ -spin site energies become disordered, reflecting both Coulombic disorder in the bare site energies and disorder in the distribution of local charges and moments; see Eq. (17). Nonetheless, for interaction strengths up to $U=5$ eV, the above general picture is found to remain essentially unchanged. Centrally, however, a further increase in U up to 6.5 eV and beyond results, for all x considered, in the formation of a pseudogap at E_F , which broadens and deepens with increasing U . Figure 2 shows the resultant CB quasiparticle DOS at $U=6.5$ eV and $0.05 \leq x \leq 0.60$, obtained from spectrum slicing with a resolution of 6 meV which is of the order of the finite-size fluctuations at the respective system sizes; this fine resolution is needed to fully pick up the pseudogap especially at the smallest doping levels 0.05 and 0.10. Most importantly, it allows for comparison with experimental tunneling conductance data. Figure 3 reproduces Fig. 19 in Ref. 5, showing the normalized tunneling conductance G as a function of the bias voltage for (A) Au-Na_{0.6}WO₃, (B) Au-Na_{0.45}WO₃, (C) Au-Na_{0.6}Ta_{0.1}W_{0.9}O₃, and (D) Au-Na_{0.34}Ta_{0.16}W_{0.84}O₃ junctions at 4.2 K; note that the curves have been shifted relative to each other for clarity. Insofar as the experimental curves are representative of the DOS near the Fermi level (which is itself quite a subtle matter; see, e.g., Ref. 30 for a discussion) good agreement is found between the numerical results and experiment for $x=0.6$ [Fig. 3(A)], with regard to both the curvature and width of the pseudogap; see Fig. 4(a) (solid line). Curve (B) in Fig. 3, together with curves (C) and (D) which correspond to tantalum-substituted tungsten bronzes at lower doping ($x-y$)=0.5 and 0.18, suggests that the pseudogap becomes more pronounced on decreasing $(x-y)$; this has also been

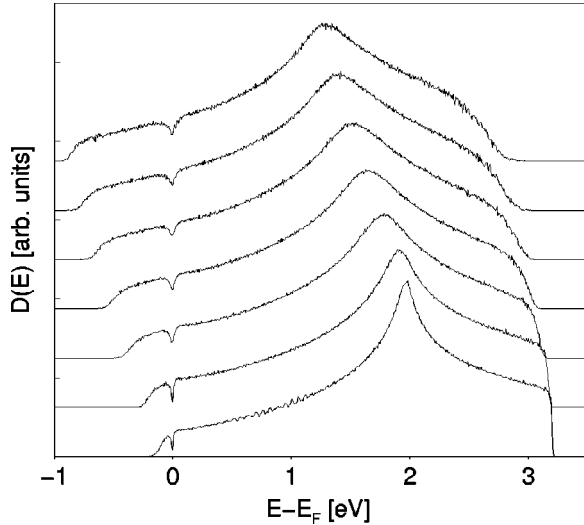


FIG. 2. CB density of states for the 2D model of Na_xWO_3 with $U=6.5$ eV, $V_C=-0.3$ eV, and (from bottom) $x=0.05, 0.10, 0.20, \dots, 0.60$. The linear dimension $L=100$ for $x \leq 0.1$; $L=70$ otherwise.

inferred from CB photoemission^{31–33} of Na_xWO_3 and $\text{Na}_x\text{Ta}_y\text{W}_{1-y}\text{O}_3$ samples. In our numerical spectra the DOS at E_F indeed decreases with decreasing x . The width of the pseudogap is, however, found to narrow slightly with diminishing x at fixed U . This is in contrast to experiment, although readily explained by invoking an x -dependent $U(x)$ that increases with decreasing x , as one indeed expects physically due to screening of the Coulomb interaction. More importantly, the results, together with those for $U=7.5$ and 10 eV, show that linear pseudogap edges are compatible with our model. This is illustrated in Fig. 4(b) (dashed line), showing the pseudogap for $U=10$ eV and $x=0.4$. We note in passing that tantalum substitution has no further significant effect on the pseudogap shape as will be shown in Sec. V.

We now turn to the localization properties of CB quasi-particle states, especially those in the vicinity of E_F which are relevant for the MIT. How does the pseudogap affect the localization properties of these states? For later comparison,

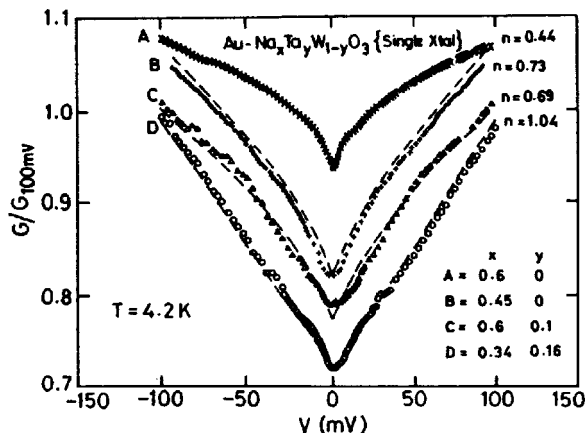


FIG. 3. Reproduction of Fig. 19 in Ref. 5 by courtesy of Dr. A. K. Raychaudhuri and the publisher Taylor & Francis. Note that the curves have been shifted relative to each other for clarity.

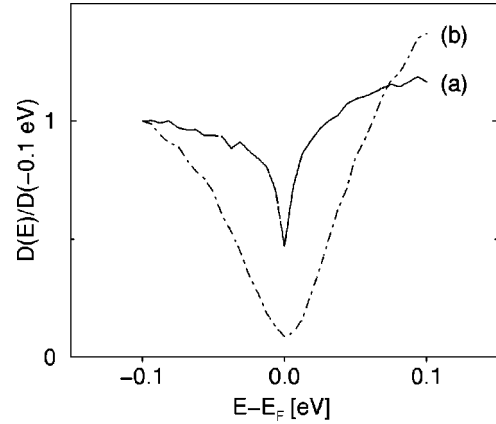


FIG. 4. Normalized CB density of states for the 2D model of Na_xWO_3 near E_F . (a) (solid line) $U=6.5$ eV, $V_C=-0.3$ eV, $L=60$, and $x=0.60$. (b) (dashed line) $U=10$ eV, $V_C=-0.3$ eV, $L=50$, and $x=0.40$.

and to clarify the numerical analysis, it is instructive to consider first a system without a pseudogap. To this end, Fig. 5 shows a scatter plot of the energy-dependent renormalized correlation length $\mathcal{L}_{\alpha\sigma}^{(1)}$ [see Eq. (20)] for $U=5.0$ eV, $V_C=-0.3$ eV, and $x=0.30$. Statistics have been gathered from 25 disorder realizations with 3600 tungsten atoms. Significantly, a fairly sharp crossover from strongly to weakly localized states with increasing energy is observed, and the correlation length of weakly localized states is virtually that of Bloch states ($\mathcal{L}_{\alpha\sigma}^{(n)}=1.0$) in this relatively large system; this general trend is also found in systems that exhibit a pseudogap.

More quantitative information on localization properties is obtained from the system-size scaling of $\mathcal{L}^{(1)}$, shown in Fig. 6 for the same parameters. The energy scale is divided into bins of width 0.05 eV and, in each bin, the renormalized correlation length is plotted for systems of linear dimensions $L=30, 40, 50$, and 60 W atoms (from left to right). If $\mathcal{L}^{(1)}$ decreases with L , the states are deemed localized, while if it increases or stays constant, the states are weakly localized.⁵⁹ It is clear that the system-size scaling corroborates the qualitative analysis of the scatter plot. From Fig. 6 it is clear that the Fermi level lies in a region of very weakly localized states. We anticipate (and find below) that the introduction of

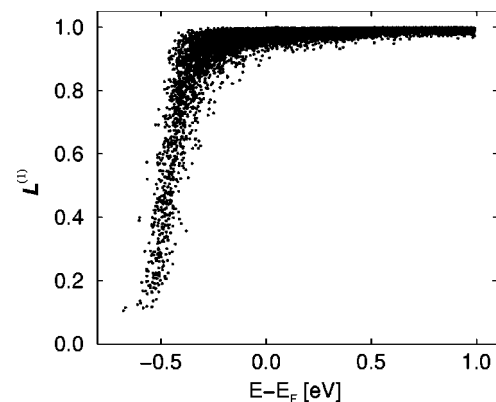


FIG. 5. Scatter plot of the renormalized correlation length $\mathcal{L}^{(1)}$ for $U=5.0$ eV, $V_C=-0.3$ eV, $x=0.30$, and $L=60$ for the 2D model of Na_xWO_3 .

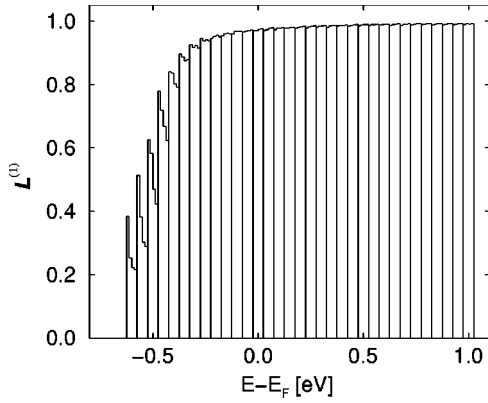


FIG. 6. Scaling behavior of the renormalized correlation length $\mathcal{L}^{(1)}$ for the 2D model of Na_xWO_3 for $U=5.0$ eV, $V_C=-0.3$ eV, system sizes $L=30, 40, 50,$ and 60 (from left to right in each energy bin of width 0.05 eV), and $x=0.30$; see text.

a small interplane coupling will render these very weakly localized states extended, while more strongly localized states will remain thus;⁶² i.e., the crossover between strongly and weakly localized states becomes a mobility edge in the full 3D system. We thus associate a MIT with the passing of the Fermi level into a region of very weakly localized states, as the doping level x is progressively increased. Following these lines, we position the MIT for $U=5$ eV at $x\approx 0.1$ from studies over a range of doping levels.

We now increase the interaction strength to $U=7.5$ eV. This has a profound effect on both the DOS—in which a pseudogap now arises [see also Fig. 18(a) (top)]—and on the localization characteristics, reflecting the important interplay between disorder and electron interactions. Figure 7(a) shows the renormalized correlation length $\mathcal{L}^{(2)}$ for $U=7.5$ eV (with $V_C=-0.30$ eV, $x=0.30$ again) and a system size of 2500 W atoms. While the general trend from strong to weak localization is qualitatively similar to the $U=5$ eV case, states in the pseudogap are seen to be more strongly localized than would be predicted from the overall trend. This behavior is also manifest both in the participation ratio of pseudoparticle states defined by Eq. (23), and shown

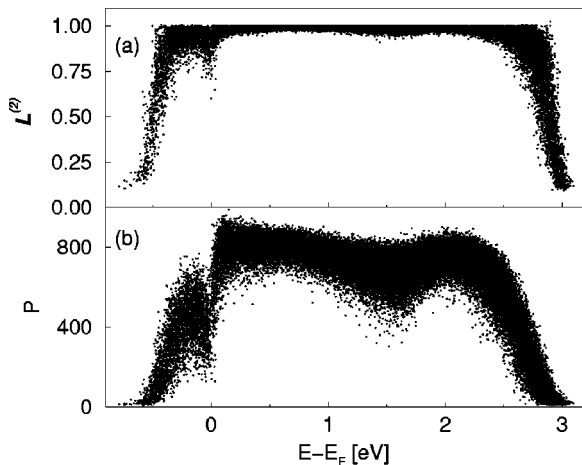


FIG. 7. (a) Scatter plot of the renormalized correlation length $\mathcal{L}^{(2)}$ for $U=7.5$ eV, $V_C=-0.3$ eV, $x=0.30$, and $L=50$. (b) Scatter plot of the participation ratio for the same parameters. The entire CB is shown.

in Fig. 7(b), and in the system-size scaling of $\mathcal{L}^{(1)}$ (Fig. 8).

While Figs. 7(a) and 7(b) each show an enhanced localization of states in the pseudogap, the two measures also exhibit important differences. Whereas $\mathcal{L}^{(2)}$ [Fig. 7(a)] attains its maximum value of 1.0 both below and above the pseudogap at E_F , indicating that the corresponding quasiparticle states are extended, the participation ratio P [Fig. 7(b)] remains well below the Bloch limit of $N=2500$. These differences occur because the participation ratio—which measures the number of sites that contribute significantly to a given single-particle state—does not contain direct information about its spatial extent, whereas the correlation length does. In interacting systems this difference can be relevant: for example, the participation ratio of the extended single-particle states of a perfect Néel antiferromagnet on a hypercubic lattice with $|\mu|=1$ is reduced by a factor of $1/2$ with respect to that of Bloch states [see Eq. (23)]. The correlation length $\Lambda_{a\sigma}^{(2)}$ by contrast is unaffected by such correlations in the limit $L\rightarrow\infty$ [see Eq. (22)], and reflects correctly the spatial extent of single-particle states. It is thus preferable to the participation ratio in the assessment of localization properties in interacting systems.

Although regions of weakly localized states exist both above and (for sufficiently large x) below E_F , it is found that for $U\geq 7.5$ eV states in the pseudogap always remain more strongly localized, regardless of x : strong electron interactions thus suppress the MIT found at $U=5$ eV, a view supported by the scaling studies of the 3D systems described below. Can then a compositionally driven MIT occur in our model at a Hubbard U large enough to yield the pseudogap observed experimentally? Figure 9 shows the system-size scaling of $\mathcal{L}^{(1)}$ for $U=6.5$ eV, $V_C=-0.3$ eV, and $x=0.05$ (a), 0.30 (b), and 0.60 (c). While at $x=0.05$ states around E_F are clearly localized, for $x=0.30$ and 0.60 the stronger localization of states in the pseudogap found at $U=7.5$ eV is almost completely lifted. In conjunction with the corresponding DOS (Fig. 2), we conclude that at $x\approx 0.6$ metallic behavior and a pseudogap that compares with experimental results can coexist within the AMH model. The critical level of doping $x_c\approx 0.3$ at $U=6.5$ eV is, however, somewhat in excess of the experimental result $x_c\leq 0.2$ and (as above) the numerical pseudogap width at low doping is slightly too small. As mentioned above, one may account for the latter by invoking screening and thus an x -dependent U , although we note that this will in addition cause increased localization of states around E_F .

We now consider the spatial distribution of quasiparticle states. It is clear from theory⁶² and experiment that the spectral properties of CB states are only marginally affected by the small matrix elements that actually render the states 3D. Neglect of these couplings enabled us to study above the formation of the pseudogap at an adequate energy resolution. However the presupposition that the localization properties of quasiparticle states in the full 3D system can be inferred from the 2D model deserves further consideration. The TB Hamiltonian is therefore extended by the addition of O-O next-nearest-neighbor π -type transfer matrix elements of magnitude $\frac{1}{6}t$, whereby only parallel planes are coupled and the one-orbital-per-site approximation is retained. In this way the model remains numerically tractable for meaningful

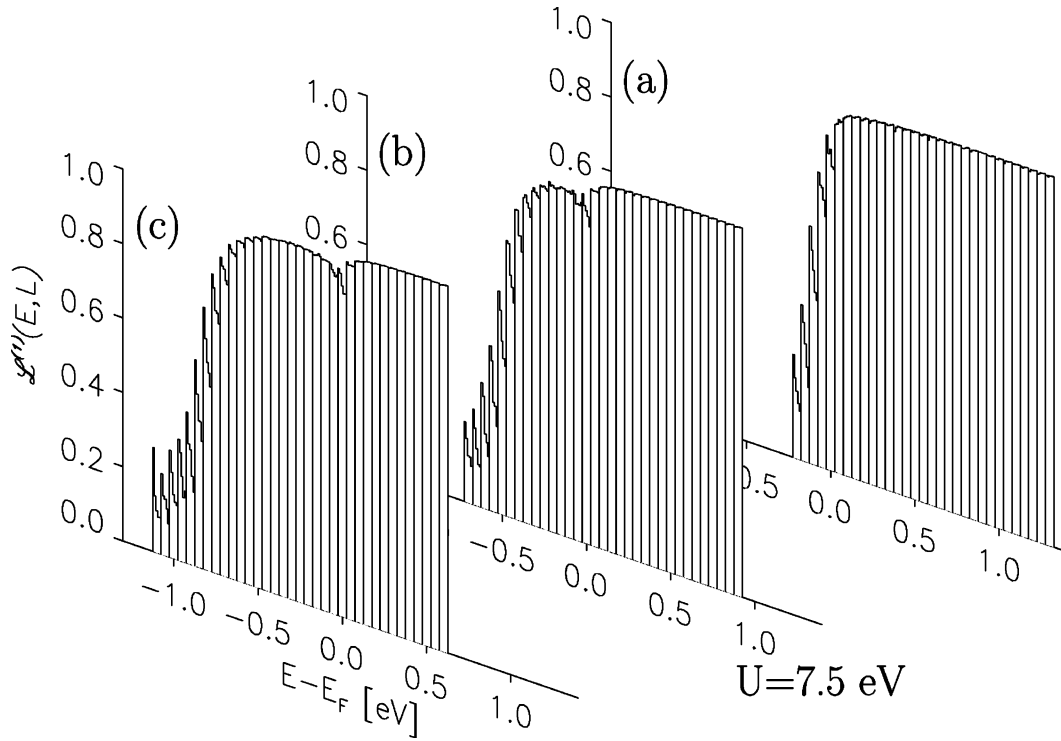


FIG. 8. Scaling behavior of the renormalized correlation length $\mathcal{L}^{(1)}$ for the 2D model of Na_xWO_3 for $U=7.5$ eV, $V_C=-0.3$ eV, system sizes of $L=30,40,50,60,70$ (from left to right in each energy bin of width 0.05 eV), and $x=0.05$ (a), $x=0.30$ (b), and $x=0.60$ (c) (from back to front); for details see text.

system sizes. It should also be emphasized that we seek here to address aspects of dimensionality, and not to refine the band structure. Most significant are the localization characteristics of quasiparticle states, as inferred from system-size

scaling of $\mathcal{L}^{(n)}$. This can no longer be done in an entirely satisfactory way, however, since systems large enough to eliminate degeneracy effects cannot yet be handled even on large vector computers, despite the approximations that have

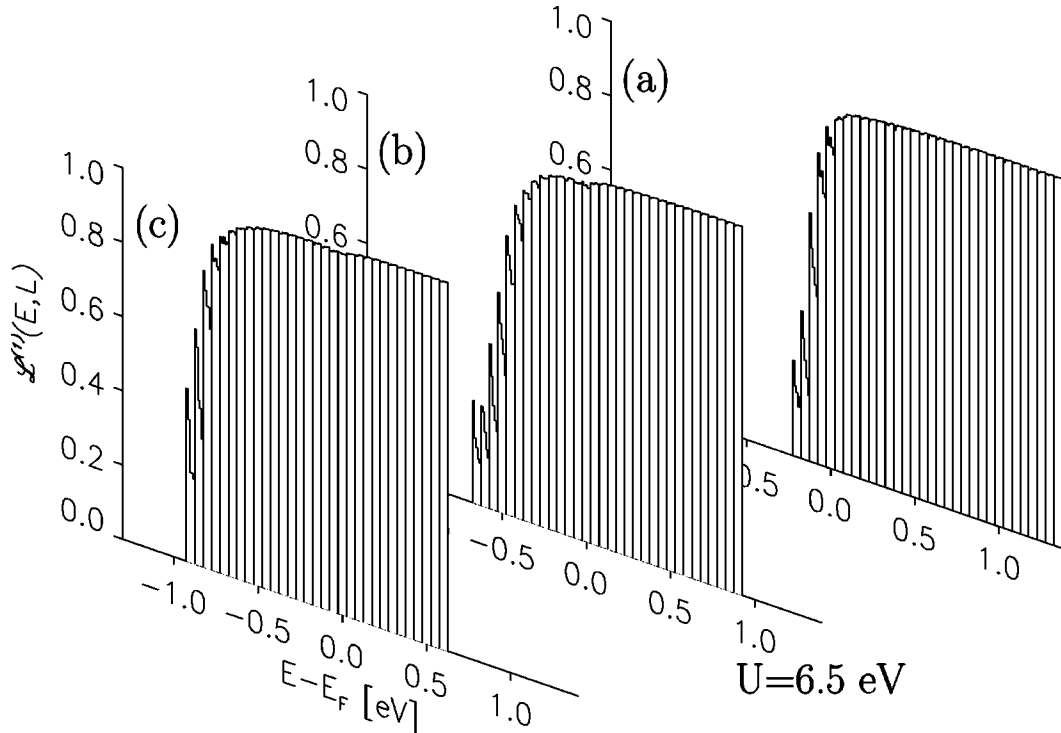


FIG. 9. Scaling behavior of the renormalized correlation length $\mathcal{L}^{(1)}$ for the 2D model of Na_xWO_3 for $U=6.5$ eV, $V_C=-0.3$ eV, system sizes of $L=30,40,50,60,70$ (from left to right in each energy bin of width 0.05 eV), and $x=0.05$ (a), $x=0.30$ (b) and $x=0.60$ (c) (from back to front).

been made. We thus pursued two alternative approaches: (a) four planes, enlarging the number of unit cells per plane from 30^2 to 50^2 ; (b) 30^2 unit cells per plane with coupling of $K=4, 6, 8,$ and 10 planes. Procedure (a) is found to support the assumption above that strongly localized states in the strictly 2D system remain so in the 3D model, while very weakly localized states become extended. In case (b), which corresponds to system-size scaling solely in the direction perpendicular to the planes, the renormalized correlation length of states which were very weakly localized in the 2D system—though close to unity—decreases very slightly with increasing number of planes. This behavior, coupled with the results of procedure (a), suggests strongly that these highly anisotropic states are extended in the plane and decay weakly in the perpendicular direction, as considered in detail below. Most importantly, states within the pseudogap are found to be more strongly localized with respect to the overall trend, as in the pure 2D case.

Insight into the dimensional crossover is gained from a separate summation of “in-plane” and “out-of-plane” contributions to $\Lambda^{(2)}$ [Eq. (21)]. We define the in-plane correlation length $\Lambda^{(2,\text{ip})}$ via

$$\Lambda_{\alpha\sigma}^{(2,\text{ip})} = \left(\frac{\sum_{k=1}^K \sum_{i,j}'' |a_{i\alpha\sigma}|^2 |a_{j\alpha\sigma}|^2 r_{ij}^2}{(q_{\alpha\sigma}^W)^2} \right)^{1/2}, \quad (24)$$

where the index k runs over all planes and the double prime denotes a sum over tungsten sites within the k plane only; the corresponding $\Lambda_{\text{Bloch}}^{(2,\text{ip})}$ is given by $a\sqrt{(L^2+2)/(6K)}$ and thus decreases for fixed L with increasing numbers of planes, K . The complementary out-of-plane correlation length $\Lambda^{(2,\text{op})}$ is obtained from a sum over pairs of tungsten sites belonging to different planes, and

$$\Lambda_{\text{Bloch}}^{(2,\text{op})} = a \sqrt{\frac{L^2+2}{6} \left(1 - \frac{1}{K} \right) + \frac{1}{2} \frac{K^2+2}{6}}. \quad (25)$$

$\Lambda^{(2,\text{op})}$ is shown in Fig. 10(a) for $U=7.5$ eV, $L=30$, $K=8$, and $x=0.60$, together with $\Lambda_{\text{Bloch}}^{(2,\text{op})}$ (dashed horizontal line); it is found to exhibit similar behavior as the total correlation length $\mathcal{L}^{(2)}$. Consider, by contrast, the corresponding energy dependence of $\Lambda^{(2,\text{ip})}$ shown in Fig. 10(b) for the same parameters and in Fig. 10(c) with $K=4$; the upper dashed horizontal line designates the 2D $\Lambda_{\text{Bloch}}^{(2)}$ and the lower $\Lambda_{\text{Bloch}}^{(2,\text{ip})}$. Starting with strongly localized states at the lower band edge a rapid growth of the in-plane correlation length follows and a peak is reached which is limited by the 2D $\Lambda_{\text{Bloch}}^{(2)}$. From thereon $\Lambda^{(2,\text{ip})}$ falls off gradually to its 3D Bloch limit, with a distinct exception: the pseudogap where $\Lambda^{(2,\text{ip})}$ approaches its 2D Bloch limit. Note that this behavior occurs irrespective of the number of planes, and that the position of the low-energy peak corresponds to the energy where weakly localized states are first observed in the 2D model (cf. Fig. 8).

To investigate further the nature of a given state, we now study the contributions from individual planes to its overall weight on tungsten sites. We increase the number of planes to 20 (but are forced to reduce the plane size to 400 W atoms); the results are shown in Fig. 11. For each state, the

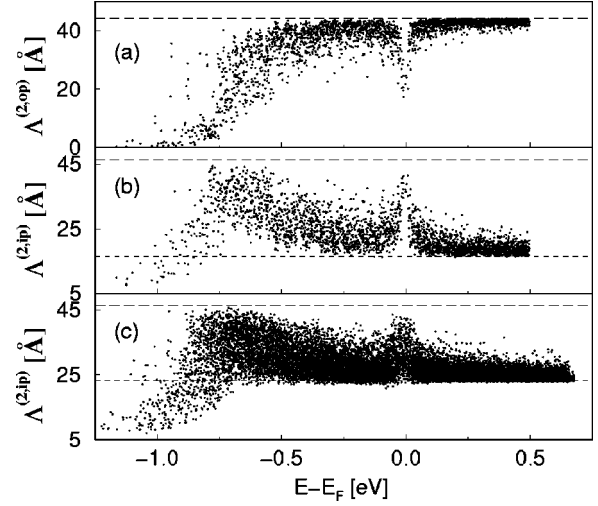


FIG. 10. (a) Scatter plot of $\Lambda^{(2,\text{op})}$ for the 3D model of Na_xWO_3 for $U=7.5$ eV, $V_C=-0.3$ eV, $x=0.60$, $L=30$, and $K=8$. The dashed horizontal line denotes $\Lambda_{\text{Bloch}}^{(2,\text{op})}$. (b) $\Lambda^{(2,\text{ip})}$, same parameters; (c) $\Lambda^{(2,\text{ip})}$, $K=4$. In (b) and (c) the dashed horizontal lines denote $\Lambda_{\text{Bloch}}^{(2)}$ for Bloch states in 2D (upper) and the 3D $\Lambda_{\text{Bloch}}^{(2,\text{ip})}$ (lower).

planes are assigned logical indices, such that the plane giving the largest contribution is numbered 20 and that giving the smallest, 1. Strongly localized states towards the lower edge of the CB are seen to be essentially confined to a single plane. Moving into the band, states gradually spread out over an increasing number of planes such that, well above E_F , states decay weakly in the direction perpendicular to the planes. Again, however, there is one notable exception: *States in the pseudogap remain strongly 2D*. Note that the observed Friedman anomaly in the T dependence of the Hall coefficient¹⁹ is consistent with this behavior. The freezing out of charge carriers at low T has been explained both in terms of a reduced DOS at E_F and localization of Fermi level states, together with thermally accessible extended states close to E_F .³⁴ These features are, of course, intimately related within the present model.

We have provided ample numerical evidence—and thus corroborated our initial hypothesis—that in this anisotropically coupled system the spatial extent of quasiparticle states is governed primarily by the 2D localization characteristics. Moreover, the 3D and 2D models do not differ in CB spectral properties, or distributions of local charge and moment magnitudes to be discussed below. In short, the original 2D model appears to be well founded. The 2D nature of localized pseudogap states revealed by the 3D model nonetheless requires further investigation, beginning with a rationalization of the physical origin of the pseudogap, to which we now turn.

We start by considering the distributions of effective σ -spin site energies $\{\epsilon_{i\sigma}\}$ [Eq. (17)]; since $H_\sigma \equiv H_{\text{UHF}}(\{\epsilon_{i\sigma}\})$, the latter ultimately govern the properties of the UHF ground state and reflect the self-consistent, inhomogeneous distribution of local charges and moments over the sites. Although these distributions tell us nothing *per se* about correlations between the effective site energies (which will be crucial in understanding the microscopic origin of the pseudogap), they do reveal the first effects of Coulomb in-

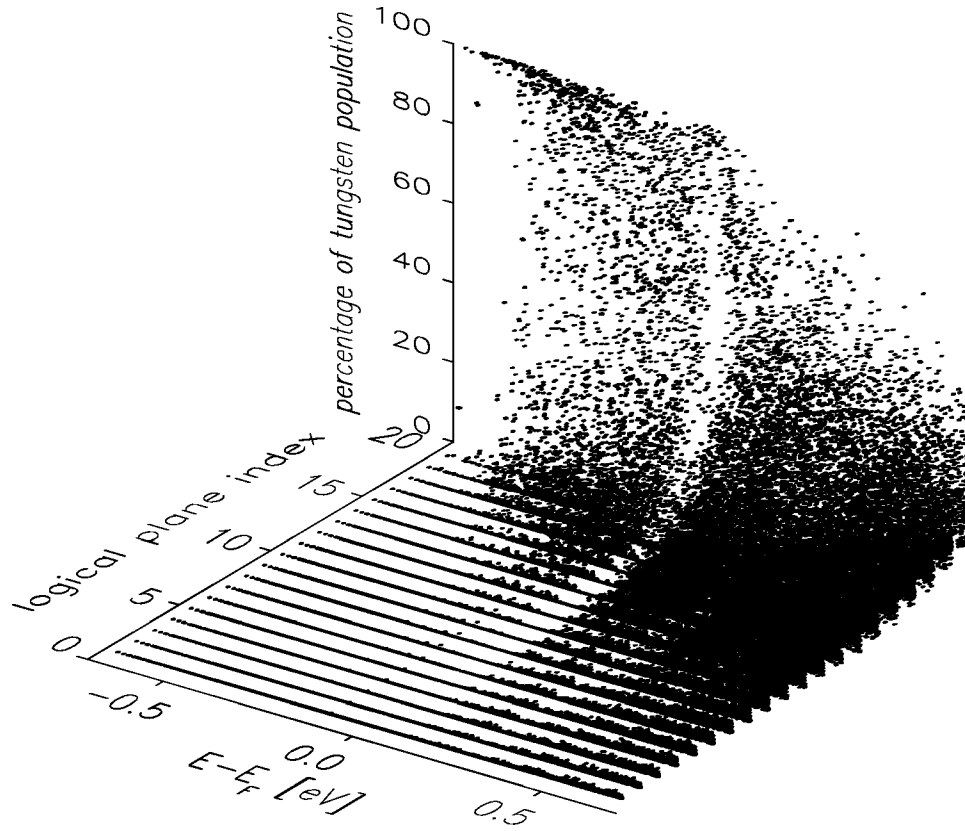


FIG. 11. Distribution of tungsten population over logical planes vs energy for the 3D model of Na_xWO_3 with $U=7.5$ eV, $V_C=-0.3$ eV, and $x=0.30$ ($L=20$, $K=20$); for details, see text.

interactions on the effective disorder and, in addition, allow a simple interpretation of, e.g., pseudoparticle spectra in certain parameter regimes.^{52,63}

Figure 12 shows the (normalized) distributions of effective tungsten site energies $f(\epsilon_{i\sigma})$, for $U=0.0$, 5.0, 7.5, and

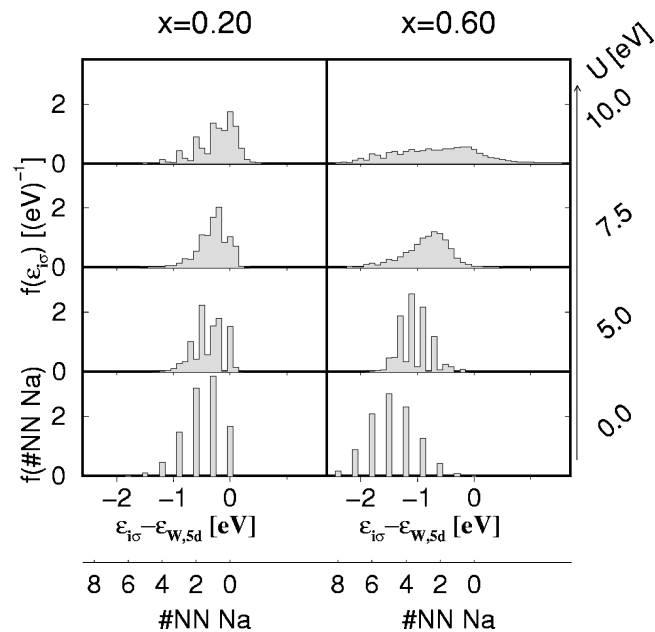


FIG. 12. Distribution of effective tungsten site energies $f(\epsilon_{i\sigma})$ for (from bottom) $U=0.0$, 5.0, 7.5, and 10.0 eV, $V_C=-0.3$ eV, and $x=0.20$ (left) and 0.60 (right); see text.

10.0 eV (from bottom), with $V_C=-0.3$ eV and $x=0.20$ (left) and $x=0.60$ (right). At $U=0$, $f(\epsilon_{i\sigma})$ is equivalent to the distribution of bare site energies $f(\epsilon_i)$; this in turn is equal to the distribution of tungsten sites with a given number of NN sodium ions $f(\#\text{NN Na})$, if the latter are represented by the cutoff Coulomb potential. As evident from Fig. 12, the fraction of low-energy sites is considerably reduced for $U=5.0$ and 7.5 eV, and the effective width of $f(\epsilon_{i\sigma})$ is narrower than that of $f(\epsilon_i)$: the low-energy sites are thus screened by the Coulomb interaction and the effective disorder is reduced. Accordingly, the CB width is first found to narrow upon raising U from 0. The screening is particularly effective at $U=5$ eV, since a further increase in the interaction strength leads to increasingly significant spin polarization which ultimately enhances the effective disorder. This is evident from Figs. 13 and 14 which show the mean local charge \bar{n}_i and mean local moment magnitude $|\bar{\mu}_i|$ on tungsten sites with a given number of NN sodium ions (Fig. 13), and the distributions of local charge and moment magnitudes (Fig. 14); in each case for $V_C=-0.3$ eV, with $U=5.0$, 6.5, 7.5, and 10.0 eV (from bottom) and $x=0.20$ (left) and $x=0.60$ (right). At $U=10$ eV the near complete spin polarization enhances the effective disorder as is evident from $f(\epsilon_{i\sigma})$ (Fig. 12), leading as found above to localization of quasiparticle states throughout the lower part of the conduction band. Note, however, that at $U=6.5$ —which value is most relevant for tungsten bronzes—the great majority of sites carries very small moments.

The above results also provide a natural explanation for observed Knight shifts. In order to explain ^{183}W NMR line

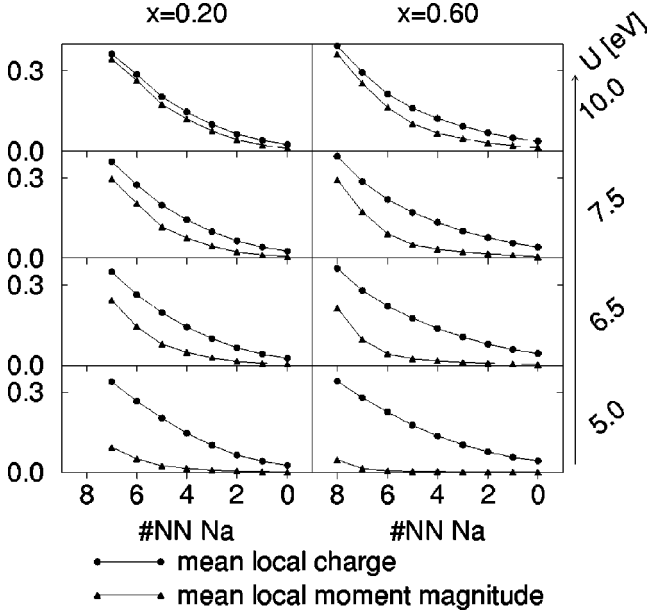


FIG. 13. Mean local charge \bar{n}_i and mean local moment magnitude $|\bar{\mu}_i|$ on tungsten sites with a given number of NN sodium ions for (from bottom) $U = 5.0, 6.5, 7.5,$ and 10.0 eV, $V_C = -0.3$ eV, and $x = 0.20$ (left) and 0.60 (right).

shapes in metallic $\text{Na}_x\text{Ta}_y\text{W}_{1-y}\text{O}_3$, Dubson and Holcomb⁶⁴ have argued that the ^{183}W Knight shifts $K = \{K_i\}$ are proportional to the local charges: $K_i \propto n_i$ (K is negative with respect to the reference signal of WO_3 since inner shell core polarization is the dominant coupling mechanism in the d band). They postulate that n_i is proportional to the number of NN sodium ions minus the number of NN tantalum atoms, where in Na_xWO_3 the NMR line shape is expected to reflect the distribution of the number of NN sodium ions $f(\#\text{NN Na})$. In this way Dubson and Holcomb have ac-

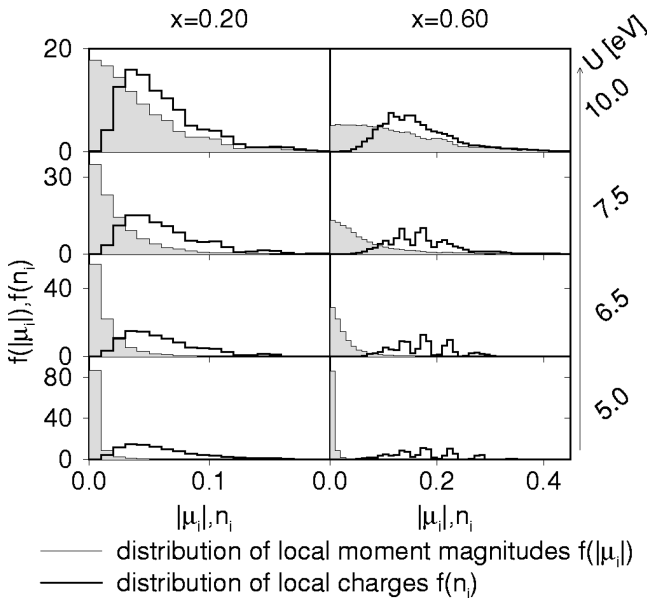


FIG. 14. Distributions $f(n_i)$ and $f(|\mu_i|)$ (shaded) of local charge and magnetic moment magnitudes for (from bottom) $U = 5.0, 6.5, 7.5,$ and 10.0 eV, $V_C = -0.3$ eV, and $x = 0.20$ (left) and 0.60 (right).

counted for the asymmetric line shape of $\text{Na}_{0.24}\text{WO}_3$ which is skewed to small $|K|$ values, for the near-symmetric line shape of $\text{Na}_{0.60}\text{WO}_3$, and for the relative peak positions. From Figs. 13 and 14, and corresponding results for $0.05 \leq x \leq 0.60$, our model is entirely compatible with the observations. With the assumption that $K_i \propto n_i$, the Knight shift distribution and hence NMR line shape is proportional to the local charge distribution, $f(n_i)$, shown in Fig. 14. From this it is evident that for $x = 0.2$ the line shape is indeed asymmetric and skewed to low n_i , while for $x = 0.6$, by contrast, $f(n_i)$ is essentially symmetrically distributed and centered on higher n_i [the irregularity in $f(n_i)$ at lower U for $x = 0.6$ reflects simply the discrete nature of the cutoff Coulomb potential, and is entirely removed if a Yukawa potential is employed]. Likewise Fig. 13 shows that \bar{n}_i increases monotonically with the number of NN Na ions, in a close to linear fashion. Finally, it is found experimentally that the peak of the ^{183}W NMR signal in $\text{Na}_{0.24}\text{WO}_3$ virtually coincides with the signal of WO_3 . This is also in agreement with our results, since at $x = 0.2$ the great majority of sites are found to carry only a very small additional charge to that of pure WO_3 .

IV. EVOLUTION OF THE PSEUDOGAP

The preceding results are not of course sufficient by themselves to explain the formation of a pseudogap, whose existence has been shown above to have a profound effect on the properties of single-particle excitations near the Fermi level E_F . Since this problem is central to the MIT, it is now examined in detail. We begin by considering a one-band AMH model. There are two reasons for this: first, because the microscopic origins of a gap or pseudogap are most clearly seen at this simplest of levels and, second, because the 2D three-band model we consider may be mapped with high accuracy onto an underlying effective one-band model, as subsequently explained.

Consider a generic site-disordered one-band AMH model on a hypercubic lattice in d dimensions,

$$\hat{H} = \sum_{i,\sigma} \epsilon_i \hat{n}_{i\sigma} + t \sum_{\langle ij \rangle, \sigma} \hat{c}_{i\sigma}^\dagger \hat{c}_{j\sigma} + \frac{1}{2} U \sum_i \hat{n}_{i\sigma} \hat{n}_{i-\sigma}; \quad (26)$$

in the Ising spin UHF approximation,

$$\hat{H} = \sum_{\sigma} \hat{H}_{\sigma},$$

$$\hat{H}_{\sigma} = \sum_i \epsilon_{i\sigma} \hat{n}_{i\sigma} + t \sum_{\langle ij \rangle} \hat{c}_{i\sigma}^\dagger \hat{c}_{j\sigma}, \quad (27)$$

with effective σ -spin site energies given by Eq. (17). The canonical transformation

$$\hat{c}_{\mathbf{k}\sigma} = \frac{1}{\sqrt{N}} \sum_i e^{i\mathbf{k} \cdot \mathbf{r}_i} \hat{c}_{i\sigma}, \quad (28)$$

which diagonalizes the one-band TB Hamiltonian, $t \sum_{\langle ij \rangle} \hat{c}_{i\sigma}^\dagger \hat{c}_{j\sigma}$, is now applied to the Ising spin UHF Hamiltonian, whereupon \hat{H}_{σ} is given by

$$\hat{H}_\sigma = \sum_{\mathbf{k}} E(\mathbf{k}) \hat{n}_{\mathbf{k}\sigma} + \sum_{\mathbf{k}, \mathbf{q}} \Gamma_\sigma(\mathbf{q}) \hat{c}_{\mathbf{k}\sigma}^\dagger \hat{c}_{(\mathbf{k}+\mathbf{q})\sigma}. \quad (29)$$

Here,

$$E(\mathbf{k}) \equiv -2t \sum_{i=1}^d \cos(k_i a) \quad (30)$$

is the TB energy dispersion, with $\hat{n}_{\mathbf{k}\sigma} \equiv \hat{c}_{\mathbf{k}\sigma}^\dagger \hat{c}_{\mathbf{k}\sigma}$ the usual number operator, and the structure factor of the effective σ -spin site energies,

$$\Gamma_\sigma(\mathbf{q}) \equiv \frac{1}{N} \sum_i \epsilon_{i\sigma} e^{i\mathbf{q} \cdot \mathbf{r}_i}, \quad (31)$$

is thus defined. Given a distribution of effective site energies over the sites, Eq. (29) shows that the structure factor $\Gamma_\sigma(\mathbf{q})$ acts to couple TB states; the coupling naturally depends only on the difference \mathbf{q} of the associated crystal momenta.

To understand the formation of a pseudogap we thus have to consider the TB energy dispersion $E(\mathbf{k})$ in conjunction with $\Gamma_\sigma(\mathbf{q})$. From Eq. (17), the latter can itself be expanded in terms of the structure factors of the bare site energies [$\Gamma_\epsilon(\mathbf{q})$], local charges [$\Gamma_n(\mathbf{q})$], and local moments [$S_z(\mathbf{q})$], to give

$$\Gamma_\sigma(\mathbf{q}) = \Gamma_\epsilon(\mathbf{q}) + \frac{1}{2} U [\Gamma_n(\mathbf{q}) - \sigma S_z(\mathbf{q})]. \quad (32)$$

Clearly, a completely random $\Gamma_\sigma(\mathbf{q})$ cannot yield a pseudogap: disorder-induced random couplings between TB states lead simply to the trivial effects of broadening and blurring of the TB DOS. To produce a pseudogap, $\Gamma_\sigma(\mathbf{q})$ must exhibit a \mathbf{q} -dependent structure which reflects spatial correlations among the effective site energies; moreover, since the pseudogap tracks E_F , this structure must depend on the filling fraction of the band.

A good example to illustrate these principles is the non-disordered limit (the pure one-band Hubbard model) at half-filling. For $d > 1$, the ground state of the model possesses antiferromagnetic (AF) long-ranged order, and a nonzero band gap, for any finite U . Both features are correctly captured by UHF. In this case $\Gamma_\sigma(\mathbf{q})$ is strictly nonrandom, due to the perfect magnetic ordering and uniformity of the local charges n ($=1$) and bare site energies ϵ : $\Gamma_\sigma(\mathbf{q}) = -(1/2)\sigma U S_z(\mathbf{q}) = -(1/2)\sigma U |\mu| \delta_{\mathbf{q}, \boldsymbol{\pi}}$, where E_F has been set to zero (i.e., $\epsilon = -U/2$). To connect the structure in $S_z(\mathbf{q})$ to the formation of a gap at E_F , note that the AF ordering vector $\boldsymbol{\pi}$ is also the nesting vector of the TB Fermi surface at half-filling. For concreteness consider $d=2$, where at half-filling the TB Fermi surface $E(\mathbf{k})=0$ is a square with side length $|\boldsymbol{\pi}| = |(\pi/a)(1,1)|$. From Eq. (29), each \mathbf{k} state within the magnetic Brillouin zone (MBZ) (i.e., each *occupied* TB state) is thus coupled to a state $\mathbf{k} + \boldsymbol{\pi}$ outside the MBZ (i.e., an *unoccupied* TB state). This perfect repulsion reflects an optimal balance between the constraints of interaction energy minimization and kinetic energy maximization. It leads self-consistently to $|\mu| \neq 0$ and, most importantly, to a band gap of magnitude $U|\mu|$ containing the Fermi level, for all $U > 0$; this is directly evident from the self-consistent Fock matrix corresponding to Eq. (29):

$$\hat{H}_\sigma = \sum_{\mathbf{k} \in \text{MBZ}} \hat{H}_{\mathbf{k}\sigma} = \bigoplus_{\mathbf{k} \in \text{MBZ}} \begin{pmatrix} E(\mathbf{k}) & -\frac{1}{2}\sigma U |\mu| \\ -\frac{1}{2}\sigma U |\mu| & E(\mathbf{k} + \boldsymbol{\pi}) \end{pmatrix} \\ = \bigoplus_{\mathbf{k} \in \text{MBZ}} \begin{pmatrix} E(\mathbf{k}) & -\frac{1}{2}\sigma U |\mu| \\ -\frac{1}{2}\sigma U |\mu| & -E(\mathbf{k}) \end{pmatrix}, \quad (33)$$

where \oplus denotes a direct sum. Note that the formation and position of the gap are controlled by correlations between the effective site energies, which in turn are governed by the shape of the TB Fermi surface.

The essential characteristics of the above picture at half-filling are robust to the inclusion of disorder.⁵² In general a strict gap naturally no longer occurs, disorder smearing the gap to produce a pseudogap containing E_F . Nonetheless, as known from study of the 3D half-filled Gaussian site-disordered AMH model,⁵² a pseudogap remains characteristic of the disordered antiferromagnetic phases of the AMH (including both insulating and metallic regimes), indicating the broad significance of the above repulsion mechanism.

Away from half-filling the nesting property of the underlying TB Fermi surface is of course lost. Nevertheless, in disordered interacting systems, AF correlations occurring on doping dependent length scales may still act to repel states on opposite sides of the Fermi surface: this is the microscopic origin of the pseudogap in our model, as now shown. To this end we adopt the same strategy as in the example of the one-band AMH model above; i.e., the three-band Ising spin UHF Hamiltonian is evaluated in a \mathbf{k} -space basis of TB eigenstates. Here, a sequence of three unitary transformations is required to accomplish this. In addition, physically well-motivated and accurate approximations enable the full three-band Hamiltonian to be reduced to an effective one-band model. Full technical details are given in the Appendix, and the essential physical arguments that lead to an effective one-band model are as follows.

(i) Disorder on oxygen sites is insignificant for the relevant states at the bottom of the CB due to their small oxygen population, and can thus be neglected to the extent that a nonbonding, purely oxygen-derived valence band decouples from the full Hamiltonian as in the case of the underlying TB Hamiltonian \hat{H}^{TB} [cf. Eq. (2)] discussed in Sec. II. The resultant effective two-band model for π bonding and antibonding bands is considered at the end of this section, and is found to capture very accurately the properties of CB single-particle states.

(ii) In the final step the two-band model is reduced to an effective one-band model for CB states, by neglect of matrix elements between VB and CB TB states which are small in comparison to the charge-transfer gap between valence and conduction bands.

The validity of these approximations is, of course, directly testable by comparison of results from the full three-band model with those of the effective one-band model. For example, Fig. 15 compares the resultant CB single-particle

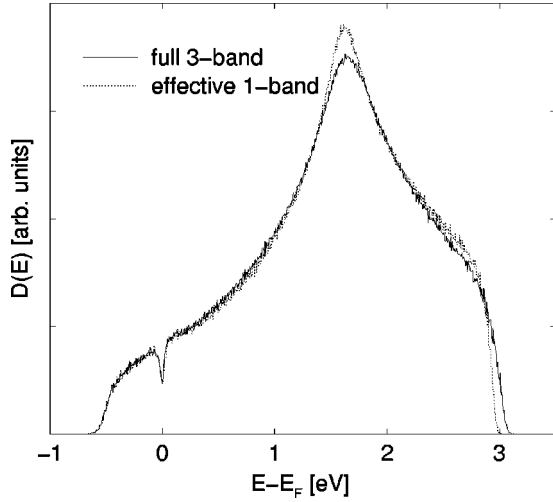


FIG. 15. CB density of states of the effective one-band (dotted line) and full three-band models. $U=6.5$ eV, $V_C=-0.3$ eV, $x=0.30$, and $L=70$.

spectra for $U=6.5$ eV and $x=0.3$. The one-band model is seen to be in excellent agreement with the full three-band model, particularly in the relevant low-energy part of the DOS.

The resultant effective one-band Hamiltonian is a direct analog of Eq. (29), and (as detailed in the Appendix), is given by

$$\hat{H} = \sum_{\sigma} \hat{H}_{\sigma},$$

$$\hat{H}_{\sigma} = \sum_{\mathbf{k}} E_{\mathbf{k}\sigma}^{+\star} \hat{n}_{\mathbf{k}\sigma}^{+\star} + \sum_{\mathbf{k}, \mathbf{q} \neq \mathbf{0}} \Gamma'_{\sigma}(\mathbf{q}) \sqrt{q_{\mathbf{k}\sigma}^{\text{W}+\star} q_{(\mathbf{k}+\mathbf{q})\sigma}^{\text{W}+\star}} \hat{c}_{\mathbf{k}\sigma}^{+\star} \hat{c}_{(\mathbf{k}+\mathbf{q})\sigma}^{+\star}. \quad (34)$$

Here, the prime denotes that the structure factor $\Gamma'_{\sigma}(\mathbf{q})$ is given by Eq. (31) with the summation over tungsten sites only, and the star indicates that CB TB states created by $\hat{c}_{\mathbf{k}\sigma}^{+\star}$ are renormalized with respect to those of the TB Hamiltonian \hat{H}^{TB} that underlies the three-band AMH model [cf. Eq. (2)]. This renormalization is simply due to a shift in the TB site energies $\epsilon_{\text{W},5d}$ and $\epsilon_{\text{O},2p}$ which reflects the average effect of disorder and interaction on the position and width of the bands. Thus, the mean effective tungsten site energies $\bar{\epsilon}_{\sigma\text{W}}$ and the mean bare oxygen site energy $\bar{\epsilon}_{\text{O}}$ are to be used in place of the Harrison parameters $\epsilon_{\text{W},5d}$ and $\epsilon_{\text{O},2p}$ in Eqs. (12) and (19) to evaluate the renormalized TB CB energy dispersion $E_{\mathbf{k}\sigma}^{+\star}$ and tungsten population $q_{\mathbf{k}\sigma}^{\text{W}+\star}$, respectively.

The above transformations have thus effected an approximate, but accurate, diagonalization of the three-band Ising spin UHF Hamiltonian. All specifics of the underlying band structure — as determined by the crystal lattice, $\bar{\epsilon}_{\sigma\text{W}}$, $\bar{\epsilon}_{\text{O}}$, and t — are now contained in the diagonal entries $E_{\mathbf{k}\sigma}^{+\star}$ of the effective one-band Hamiltonian, whose dependence on k_x and k_y is shown in Fig. 16. The combined effects of disorder and electron interaction on single-particle properties, as described in the previous section, originate from the off-diagonal elements $(q_{\mathbf{k}\sigma}^{\text{W}+\star} q_{\mathbf{k}+\mathbf{q}\sigma}^{\text{W}+\star})^{1/2} \Gamma'_{\sigma}(\mathbf{q})$ which, directly parallel to Eq. (29), act to couple the renormalized CB TB

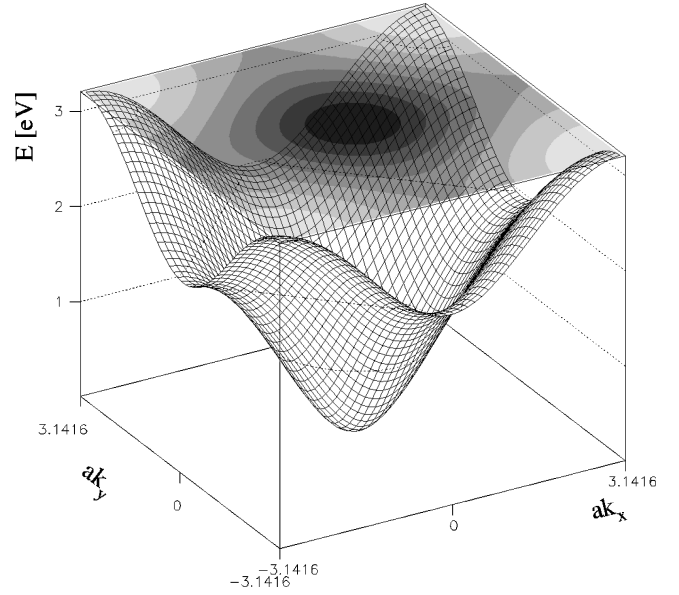


FIG. 16. CB energy dispersion of the three-band TB model. Gray-shaded contours are shown on top.

states. Here, the prefactor $(q_{\mathbf{k}\sigma}^{\text{W}+\star} q_{\mathbf{k}+\mathbf{q}\sigma}^{\text{W}+\star})^{1/2}$, i.e., the geometric mean of the renormalized TB tungsten populations of the coupled states, is largely irrelevant to the formation of the pseudogap since it is fully determined by $\bar{\epsilon}_{\sigma\text{W}}$, $\bar{\epsilon}_{\text{O}}$, and t and varies smoothly with \mathbf{k} and \mathbf{q} . Consider, however, the structure factors of the bare site energies $\Gamma'_{\epsilon}(\mathbf{q})$, local charges $\Gamma'_n(\mathbf{q})$, and moments $S'_z(\mathbf{q})$ on tungsten sites that contribute to $\Gamma'_{\sigma}(\mathbf{q})$ as in Eq. (32). $\Gamma'_{\epsilon}(\mathbf{q})$ reflects the microscopically correlated nature of the disorder potential, but does not itself lead to a pseudogap as pointed out in the previous section. $\Gamma'_n(\mathbf{q})$ [an illustrative example of which is shown in the last panel of Fig. 17(a)] is found to be barely affected by the interaction strength (cf. Fig. 13) and to be very similar to $\Gamma'_{\epsilon}(\mathbf{q})$, indicating partial screening of the disorder potential and thus partial cancellation of $\Gamma'_{\epsilon}(\mathbf{q})$ and $\frac{1}{2} U \Gamma'_n(\mathbf{q})$.

In direct analogy to the pure half-filled Hubbard model considered above, we may thus focus on the local moment structure factor $S'_z(\mathbf{q})$, whose doping dependence is shown in Fig. 17(a) for $U=6.5$ eV and $L=100$ as obtained from single disorder realizations of the 2D three-band AMH model [Eqs. (14)] via Fourier transformation of the self-consistent UHF local magnetic moments on tungsten sites. In the metallic phase $x>0.3$, $|S'_z(\mathbf{q})|$ is far from random, being peaked on a ring whose radius is the diameter $2k_F(x)$ of the TB Fermi surface: the latter is, to a very good approximation, circular in the 2D model at the relevant small filling fractions (and square at half-filling); see Fig. 16. As in the example of the half-filled Hubbard model, therefore, the TB Fermi surface thus determines the spatial correlations between TB states below the TB Fermi surface while maximizing repulsion between states on opposite sides, hence leading again to a pseudogap at E_F , and the largest total energy gain within the variational UHF procedure.

In the insulating regime (which is also accessible for $x>0.3$ via an increase in U), localization of states naturally

renders the Fermi surface ill defined. Correspondingly, $S'_z(\mathbf{q})$ loses its ringlike structure and becomes disklike: see Fig. 17(a). Nonetheless, the radius of this disk still evolves with $2k_F$, and the TB Fermi energy $E_{k_F\sigma}^{+*}$ remains a good estimate of the exact Fermi energy. Thus, while a \mathbf{k} -space description is inappropriate for small x and large U , one still expects persistence of the basic underlying mechanism relating local magnetic correlations to the formation of the pseudogap.

In summary, the origins of the pseudogap stem from the \mathbf{q} dependence of $\Gamma'_\sigma(\mathbf{q})$, whose evolution with both CB filling fraction and interaction strength is dominated by that of $S'_z(\mathbf{q})$, reflecting the presence of, and spatial correlation between, local moments. The latter is of an AF nature as evident from the up and down spin densities shown in Fig. 17(b). Furthermore, the characteristic $2k_F$ dependence of $S'_z(\mathbf{q})$ in turn sets an x -dependent length scale for spatial correlation between the moments. At half-filling, for example, the nesting vector $\boldsymbol{\pi}$ corresponds to antiferromagnetic coupling on the shortest possible length scale, i.e., between NN transition metal sites, while as x decreases, the AF length scale correspondingly increases as illustrated in Fig. 17(b).

Three further points should be noted. First, relatively strong local moments typically overlap clusters of tungsten sites in the vicinity of sodium ions, and while the average distance between neighboring clusters also decreases with increasing x , the relative phases of the local moments are found to be governed by the diameter of the TB Fermi surface. In consequence, the bare site energies can be randomly redistributed over tungsten and oxygen sites prior to the self-consistent UHF procedure, without any significant effect on the appearance of the local moment structure factor $S'_z(\mathbf{q})$ and the pseudogap. This serves further to show that the microscopically correlated nature of the disorder potential is not a prerequisite for the formation of a pseudogap in the model, although correlated disorder is more effectively screened than uncorrelated disorder. We add moreover that for a given disorder realization, the effect of raising U on the spin densities [Fig. 17(b)] is a sharpening of the observed patterns, which naturally reflects the enhanced localization of states and the formation of stronger moments. While this ultimately renders the \mathbf{k} -space description obsolete, the persistence and sharpening of the pattern in real space indicates, as one would expect, that the repulsion mechanism remains operative and becomes more effective, and it is this that underlies the concomitant broadening of the pseudogap seen in Fig. 4.

Second, we stress that, while a \mathbf{k} -space representation has been employed in the preceding analysis, disorder is essential in leading to local moment formation at the filling fractions and interaction strengths studied. This reflects the enhancement of electron interactions in localized single-particle states;⁵² for example, if at $U=7.5$ eV the concentration of sodium ions is artificially reduced (at fixed CB filling fraction x), local moment magnitudes decrease and the pseudogap ultimately vanishes.

Finally, we add that additional support for the above mechanism derives from the width of the pseudogap itself, which is given roughly by $U|\mu|q^{W+*}$, where $|\mu|$ is the average local moment magnitude on tungsten sites and q^{W+*} is an effective tungsten population of occupied renormalized

TB states (close to unity). This represents essentially the energy difference between spatially correlated and random local moments, and thus should occur on an meV scale characteristic of magnetic correlations as opposed to the eV scale of the Coulomb interaction, as indeed is observed experimentally.

As we have seen above, the UHF self-consistency involves mixing of renormalized TB states below the Fermi energy with higher-lying states in the conduction band. We might therefore expect it to have a significant effect on chemical bonding. In the remainder of this section we consider implications of the pseudogap for chemical bonding, as revealed by a population analysis of CB single-particle states. The results provide further numerical evidence for a band repulsion induced by magnetic correlations.

We consider the hopping operator

$$\hat{H}^{\text{hop}} \equiv \sum_{\sigma} \sum_{\langle ij \rangle} t_{ij} \hat{c}_{i\sigma}^{\dagger} \hat{c}_{j\sigma} \quad (35)$$

whose expectation value

$$\langle \hat{H}^{\text{hop}} \rangle_{\alpha\sigma} \equiv \langle \alpha\sigma | \hat{H}^{\text{hop}} | \alpha\sigma \rangle = E_{\alpha\sigma} - \sum_i \epsilon_{i\sigma} |a_{i\alpha\sigma}|^2 \quad (36)$$

is a measure of the antibonding character of CB single-particle states $|\alpha\sigma\rangle$.

The expectation value is most conveniently evaluated in the basis (8), where the matrix elements of \hat{H}^{hop} are given by Eq. (A3) and $\langle \hat{H}^{\text{hop}} \rangle_{\alpha\sigma}$ becomes

$$\langle \hat{H}^{\text{hop}} \rangle_{\alpha\sigma} = -2 \sum_{\mathbf{k}} t(\mathbf{k}) \text{Re}(a_{\mathbf{k}\alpha\sigma}^{(W)} a_{\mathbf{k}\alpha\sigma}^{(1)*}), \quad (37)$$

where $\text{Re}(\)$ denotes real part. Moreover, if disorder on oxygen sites is neglected (as justified above), the secular equations associated with the resultant two-band UHF Hamiltonian (A7) can be exploited to obtain the relations

$$\langle \hat{H}^{\text{hop}} \rangle_{\alpha\sigma} = 2 \sqrt{q_{\alpha\sigma}^O T_{\alpha\sigma}} \quad (38)$$

and

$$E_{\alpha\sigma} = \bar{\epsilon}_O + \frac{1}{2} \frac{\langle \hat{H}^{\text{hop}} \rangle_{\alpha\sigma}}{q_{\alpha\sigma}^O} \quad (39)$$

$$= \bar{\epsilon}_O + \frac{1}{2} \sqrt{\frac{T_{\alpha\sigma}}{q_{\alpha\sigma}^O}}, \quad (40)$$

where $T_{\alpha\sigma} \equiv \sum_{\mathbf{k}} t(\mathbf{k})^2 |a_{\mathbf{k}\alpha\sigma}^{(W)}|^2$ is a measure of kinetic energy and $q_{\alpha\sigma}^O = \sum_{\mathbf{k}} |a_{\mathbf{k}\alpha\sigma}^{(1)}|^2 = 1 - \sum_{\mathbf{k}} |a_{\mathbf{k}\alpha\sigma}^{(W)}|^2 = 1 - q_{\alpha\sigma}^W$ is the oxygen population of the CB state $|\alpha\sigma\rangle$. Maximum information can thus be gained if $T_{\alpha\sigma}$ and $q_{\alpha\sigma}^O$ are evaluated separately.

We have adopted two specific numerical schemes in order to obtain the requisite expansion coefficients $a_{\mathbf{k}\alpha\sigma}^{(W)}$.

(i) Approximate single-particle states are retrieved from a single Lanczos diagonalization after the oxygen site energies of a given converged UHF configuration have been replaced by their average value $\bar{\epsilon}_O$.

(ii) UHF calculations are performed using a common oxygen site energy $\bar{\epsilon}_O$ from the outset.

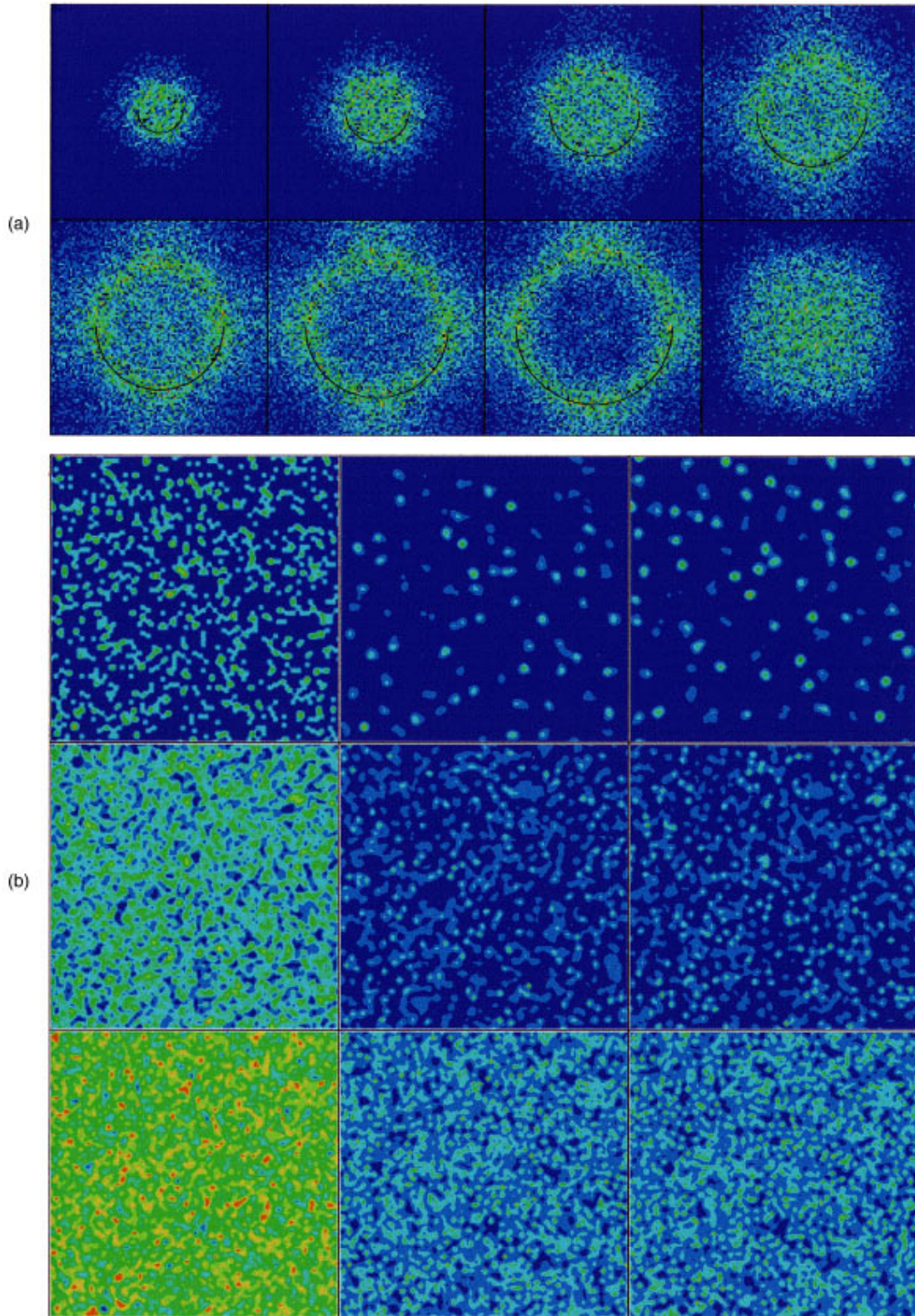


FIG. 17. (Color) (a,top) Color encoded plots of $|S'_z(\mathbf{q})|$ for $U=6.5$ eV, $V_C=-0.3$ eV, $L=100$, and (rowwise from top left) $x=0.05, 0.10, 0.20, \dots, 0.60$. A half-circle of radius $2k_F$ is also shown as a black solid line. k_F has been calculated from the requirement that the resultant circle encompass $4 \times N_{\text{occ}}$ \mathbf{q} points, where N_{occ} is the number of occupied CB states. The last panel in the bottom row shows the modulus of the structure factor of the local charges $|\Gamma'_n(\mathbf{q})|$ at $x=0.60$. The mean local charge has been set to zero. (b,bottom) Color encoded contours of the bare site energies (left) and up- and down-spin densities $\bar{n}_{i\sigma}$ on tungsten sites for $U=6.5$ eV, $V_C=-0.3$ eV, $L=100$, and $x=0.05$ (top), $x=0.30$ (middle), and $x=0.60$ (bottom). All data derive from the 2D three-band AMH model.

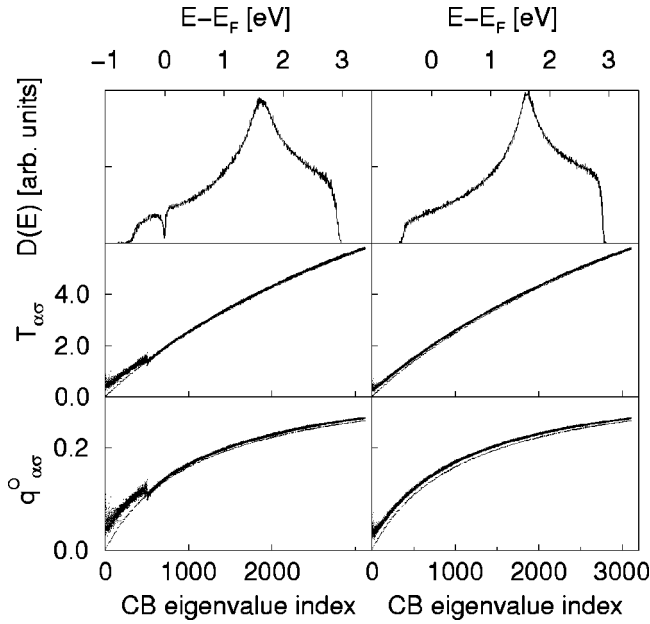


FIG. 18. CB oxygen population (bottom), $T_{\alpha\sigma}$ (middle), and DOS (top) for $U=7.5$ eV, $V_C=-0.3$ eV, $x=0.30$, and $L=100$. (a) (left) correlated and (b) (right) scrambled tungsten effective site energies (see text). In the top and middle panels the TB analogs are also shown.

In both cases the coefficients $a_{\mathbf{k}\alpha\sigma}^{(W)}$ follow from a fast Fourier analysis applied to the subset of tungsten eigenvector components $\{a_{i\alpha\sigma}\}$ of each single-particle state.

The single-particle properties obtained from these two procedures (i.e., DOS, oxygen populations, and localization characteristics) are found to be in excellent agreement with results of the full model. Moreover, the approximate single-particle energies $E_{\alpha\sigma}$ of approach (i) virtually coincide with the exact values for states at the bottom of the conduction band. We attribute the insignificance of disorder in the oxygen site energies to the small oxygen population of occupied CB states and note that, for the same reason, incorporation of a realistic Hubbard U on oxygen sites is likely to have a negligible effect.

In Fig. 18(a) we show results derived from approach (i) above for $U=7.5$ eV, $x=0.30$, and $L=100$. These should be compared with those of Fig. 18(b), in which for each disorder realization and spin the self-consistent UHF configurations $\{(\mathbf{r}_i, \epsilon_{i\sigma}), i \in W\}$ have been scrambled prior to procedure (i). This eliminates any spatial correlations and, therefore, the \mathbf{q} -dependent repulsion discussed above. The Hamiltonian is then that of a two-band Anderson model with tungsten site energies drawn randomly from the distribution of self-consistent effective tungsten site energies. Figure 18(b) shows that the pseudogap disappears entirely upon scrambling, and that the conduction band *narrows*, even though the removal of spatial correlations corresponds in effect to an increase in disorder.

Figure 18(b) shows the general effect of disorder on chemical bonding at the bottom of the conduction band: both $T_{\alpha\sigma}$ and $q_{\alpha\sigma}^O$ (and thus $\langle \hat{H}^{\text{hop}} \rangle_{\alpha\sigma}$) are enhanced with respect to their renormalized TB analogs $T_{\mathbf{k}\sigma}^*$ and $q_{\mathbf{k}\sigma}^{O*}$, which are also shown as solid lines. This can be understood by reverting to the effective one-band model: since TB states at the

bottom of the conduction band have nonbonding character, disorder must lead to an admixture of more antibonding states with larger q^O and T . In addition, from the disorder-induced broadening of the band, and Eq. (40), it follows that the increase in $T_{\alpha\sigma}$ is more than compensated by that in $q_{\alpha\sigma}^O$. Note that these remarks apply only to CB states beneath the central van Hove singularity (the Fermi level at half-filling).

Most importantly, Fig. 18(a) reveals marked features associated with the formation of a pseudogap. Compared with Fig. 18(b), both $T_{\alpha\sigma}$ and $q_{\alpha\sigma}^O$ are increased for occupied single-particle states and decreased for unoccupied states just above the Fermi level, indicating, respectively, more (less) antibonding character of (un)occupied states. A sharp and symmetric crossover occurs *at* the Fermi level itself. We add that these effects are not restricted to states within the pseudogap, but that *all* occupied single-particle states and a comparable number of unoccupied ones are thus affected. Additionally, $E_{\alpha\sigma}$ is generally lower for occupied single-particle states and higher for those unoccupied states, compared to the corresponding TB model, again indicative of a repulsion between TB states on opposite sides of the Fermi level. We add that this nonlocal change of the chemical bonding may also be relevant to the subsequent effects of electron-phonon interactions: it may lead to an enhancement of polaron formation by antiferromagnetic correlations, as found by Zhong and Schüttler⁶⁷ in their study of a Holstein-Hubbard model. Aspects of the possible significance of polarons in sodium tungsten bronzes have been discussed in Refs. 34, 40, 44, and 68.

V. TWO-DIMENSIONAL RESULTS FOR $\text{Na}_x\text{Ta}_y\text{W}_{1-y}\text{O}_3$

Since insulating cubic tungsten bronzes Na_xWO_3 have not been prepared, but a MIT has been reported in cubic $\text{Na}_x\text{Ta}_y\text{W}_{1-y}\text{O}_3$,¹⁸ it is of interest to study the effects of partial substitution of W by Ta. In our model, Ta sites are consistently represented by their respective Harrison parameters $\epsilon_{\text{Ta},5d}$ and t_{ij} , which leads to additional diagonal and off-diagonal disorder. For simplicity we assume that U is the same for W and Ta sites. The sodium content has been fixed at $x=0.30$ or 0.40 and UHF calculations have been performed for all possible $y < x$ in steps of 0.05 . Figure 19 shows the resultant CB DOS for $U=7.5$ eV, $V_C=0.30$ eV, $x=0.30$, and $y=0.10$, together with the associated Ta partial DOS. Also indicated are the W and Ta site energies $\epsilon_{\text{W},5d}$ and $\epsilon_{\text{Ta},5d}$. Since the latter is always considerably in excess of the Fermi level, Ta sites contribute predominantly to states at the top of the CB and have little weight in occupied CB states. The Ta local charges are thus small, and we note that the precise value of the Hubbard U on Ta sites is therefore of minor significance. At a coarse numerical resolution of 0.1 eV, Ta substitution has very little effect on the low-energy part of the CB for all U studied; this has been reported in Refs. 33 and 36. A bin width of 6 meV, however, allows for a more detailed analysis. We find a weak pseudogap with a width of roughly 30 meV already at $U=5$ eV, a feature absent in Na_xWO_3 . Figure 20 shows the DOS of $\text{Na}_{0.2}\text{WO}_3$ (dotted line) and $\text{Na}_{0.3}\text{Ta}_{0.1}\text{W}_{0.9}\text{O}_3$ for $U=7.5$ eV and $V_C=-0.3$ eV in the lower portion of the CB, i.e., for two systems with the same doping level. The width and depth of the pseudogap are slightly enhanced in

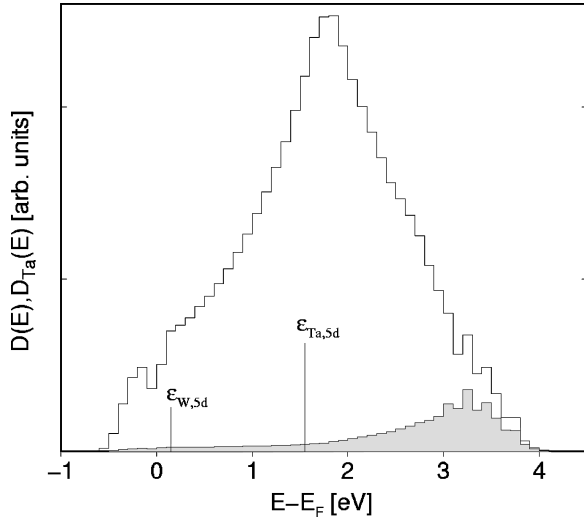


FIG. 19. CB density of states and associated Ta partial density of states for the 2D model of $\text{Na}_x\text{Ta}_y\text{W}_{1-y}\text{O}_3$ with $U = 7.5$ eV, $V_C = -0.3$ eV, $x = 0.30$, $y = 0.10$, and $L = 50$. Also indicated are the W and Ta site energies $\epsilon_{W,5d}$ and $\epsilon_{Ta,5d}$.

the substituted bronze, as is the width of the occupied part of the CB. These results indicate an enhancement of electron interactions resulting from stronger localization of pseudoparticle states in the more disordered $\text{Na}_x\text{Ta}_y\text{W}_{1-y}\text{O}_3$ system.

Semiquantitative evidence for the localizing effects of Ta substitution stems from the system size scaling of $\mathcal{L}^{(2)}$ shown in Fig. 21 for $U = 6.5$ eV, $V_C = -0.30$ eV, $(x, y) = (0.30, 0.25)$ (a), and $(x, y) = (0.30, 0.05)$ (b). Comparison of Fig. 21(a) with the corresponding Na_xWO_3 plot, Fig. 8(a), shows that states in a $\approx 1/2$ eV interval above E_F are more localized than those in the analogous Na_xWO_3 spectrum.

The existence of a zero-temperature insulating phase at $x - y = 0.05$ is clear from Fig. 21(a). However, while the additional disorder introduced by Ta substitution leads to greater localization, interaction effects remain dominant in

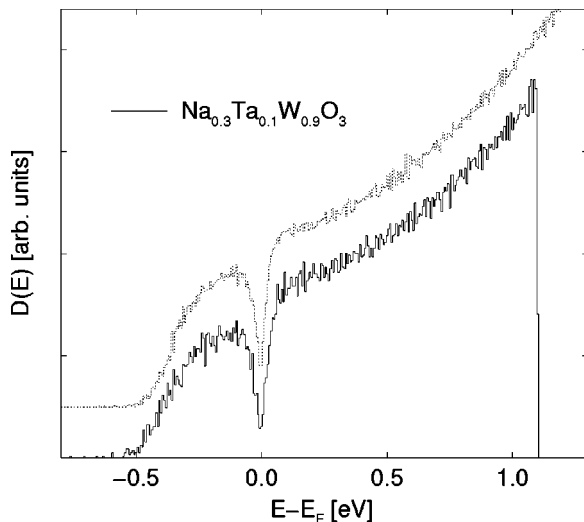


FIG. 20. CB density of states of $\text{Na}_{0.2}\text{WO}_3$ (dotted line) and $\text{Na}_{0.3}\text{Ta}_{0.1}\text{W}_{0.9}\text{O}_3$ for $U = 7.5$ eV, $L = 70$, and $V_C = -0.3$ eV in the lower portion of the CB.

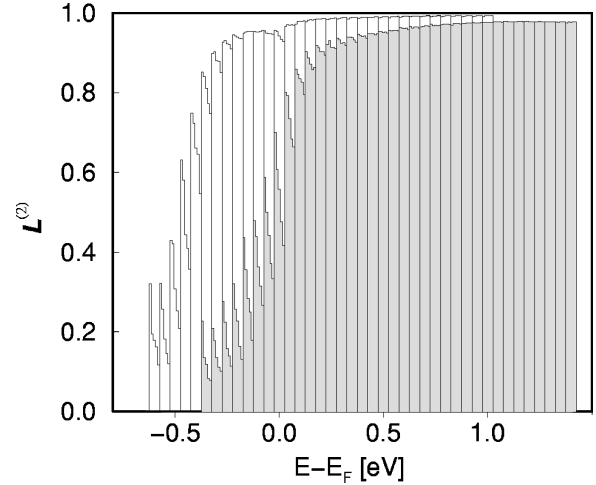


FIG. 21. Scaling behavior of the renormalized correlation length $\mathcal{L}^{(2)}$ for the 2D model of $\text{Na}_x\text{Ta}_y\text{W}_{1-y}\text{O}_3$ for $U = 6.5$ eV, $V_C = -0.3$ eV, system sizes of $L = 30, 40, 50, 60$, and 70 (from left to right in each energy bin of width 0.05 eV), and $(x, y) = (0.30, 0.25)$ (a) (shaded) and $(0.30, 0.05)$ (b).

determining the position of the MIT. The effects of additional disorder do, however, persist in the metallic phase, leading to the experimentally observed systematic reduction in the conductivity of $\text{Na}_x\text{Ta}_y\text{W}_{1-y}\text{O}_3$ compared to that of Na_xWO_3 at the same filling fraction.¹⁸

VI. DISCUSSION

The three-band AMH model combines three effects of central importance in describing transition metal oxides, namely, disorder, electron interactions, and band structure. Via a mapping of the self-consistent Hamiltonian onto an effective one-band model, we have disentangled the associated energy scales and find three mechanisms within UHF whereby the ground state energy can be minimized, viz., screening of bare site energies, the formation of local moments, and spatial correlations between them. While the precise nature and strength of the disorder potential are found to be relatively unimportant, the ground state is naturally affected most significantly by the value of U , which controls the extent of spin segregation. At $U = 6.5$ eV a rather consistent description of electronic ground state properties has emerged since the chemically induced MIT, the pseudogap, and remnants of the TB Fermi surface in the metallic phase are all well captured. The present calculations are of course confined to a mean-field level, but while a genuine many-body treatment will no doubt lead to quantitatively different results, we anticipate that the emergence of AF spin correlations and their doping-dependent length scales, which are crudely captured by the unrestricted Hartree-Fock approximation, will nonetheless remain as the underlying origin of pseudogap formation. In this regard we comment briefly on a number of additional experimental results that concur qualitatively with the picture that has emerged from our analysis.

First, a strong increase in the nuclear spin lattice relaxation rate T_1^{-1} in ^{23}Na NMR experiments on Na_xWO_3 has been observed for $x < 0.35$.^{37,69} This has variously been ascribed to a substantial (up to 56%) admixture of $\text{Na } 3s, 3p$,

or $3d$ orbitals to Fermi level states at low doping.^{37,38,69} However, a recent high-energy electron energy loss spectroscopy (EELS) study of cubic sodium tungsten bronzes¹² has shown that there is no such change in the oxidation number of sodium. We suggest that the strong increase in T_1^{-1} may reflect a considerable spin polarization of CB states, which are likely to have nonzero overlap with sodium ions since they are associated mainly with W $5d(t_{2g})$ orbitals directed along face diagonals of the cubes surrounding the latter. This explanation is consistent with the pressure dependence of the nuclear spin lattice relaxation rate:⁶⁹ significantly, under a hydrostatic pressure of 0.4 GPa, the T_1^{-1} of low- x samples is *reduced*. We would expect such an effect from a pressure-induced broadening of the $t_{2g}(\pi^*)$ conduction bands which should naturally result in less spin segregation; in contrast, it is rather more difficult to understand why a sizable admixture of sodium orbitals to CB states should decrease upon compression.

Dubson and Holcomb have found two contrary trends in their ^{183}W NMR study of $\text{Na}_x\text{Ta}_y\text{W}_{1-y}\text{O}_3$:⁶⁴ metallic samples exhibit a broad distribution of Knight shifts, reflecting the distribution of local charges (cf. Sec. III), but near-perfect exponential spin lattice relaxation which can be described by a single T_1 of $O(1s)$. Insulating bronzes by contrast have a very narrow NMR signal peaked near the reference WO_3 , and a broad distribution of spin lattice relaxation times ranging from a few seconds to more than a day. A continuous evolution of the magnetic properties across the MIT along these lines is observed. Three difficulties arise in this context.

(i) According to Dubson and Holcomb, the nuclear spin diffusion is generally suppressed due to the small moment of ^{183}W and the wide spread in local fields.⁶⁴ Thus each nucleus should relax at a rate determined by its immediate electronic environment, in apparent conflict with the single-exponential relaxation in the metallic phase.

(ii) The linewidth of insulating samples is much narrower than expected from a broad distribution of local environments.

(iii) Dubson and Holcomb argue that a population of local magnetic moments produces a *mean* internal field which would shift the peak position of the NMR line to higher frequencies. Since this is not observed, they rule out the existence of moments in this system.

We believe the following scenario is consistent both with these observations and our results: In the metallic phase the nuclear spin system is exponentially relaxed via couplings to AF fluctuations in the CB. As the MIT is approached, nuclei associated with low-energy sites experience a strong *local* field due to local moment formation, and their resonance is in effect projected out of the NMR spectrum. The NMR line is thus progressively reduced to the resonance of high-energy sites, which is near to that of WO_3 due to the small associated CB charges.

Finally, AF correlations in the CB of sodium tungsten bronzes of superconducting compositions have also been invoked by Garifullin *et al.* in order to explain results of magnetic susceptibility measurements, ESR and ^{23}Na NMR experiments.^{25,39,70,71} Unfortunately these results are for tetragonal bronzes, and thus only suggestive as far as AF correlations in the cubic bronzes are concerned. However the

recent discovery of superconductivity in the vicinity of the MIT of cubic Na_xWO_3 (Ref. 24) and $\text{Na}_x\text{Ta}_y\text{W}_{1-y}\text{O}_3$ (Ref. 18) will hopefully incite further work in this direction.

VII. CONCLUSION

In summary, we have made a detailed mean-field study of the single-particle properties of the doped transition metal oxides Na_xWO_3 and $\text{Na}_x\text{Ta}_y\text{W}_{1-y}\text{O}_3$, focusing in particular on the metal-insulator transition driven by progressive filling of the WO_3 conduction band. The latter was shown to be intimately connected with the occurrence of a pseudogap in the single-particle spectrum at the Fermi level, for sufficiently large Coulomb interaction U . A physical explanation for the microscopic origins of the pseudogap has been provided by means of a generalized effective \mathbf{k} -space description of the conduction band of the disordered interacting system at arbitrary band filling, which directly connects the underlying band structure to the structure factors of the disorder potential, local charges, and local magnetic moments. While the local charges were found to essentially screen the disorder, the emergence of a distinctive magnetic structure, exhibiting antiferromagnetic correlations on characteristic length scales determined by the doping-dependent zeroth-order Fermi surface, thus indicated a \mathbf{q} -dependent repulsion between occupied and unoccupied conduction band states which produces the pseudogap and minimizes the ground state energy, a scenario further confirmed by the results of a population analysis which revealed a concomitant nonlocal change of the chemical bonding. We add that this microscopic, mean-field picture of the relationship between the pseudogap and local moment correlations is not confined to the particular model studied here: within a symmetry-broken unrestricted Hartree-Fock treatment the essential ingredients are interactions, to produce local moments, and disorder, which enhances local moment formation at the low band filling fractions characteristic of tungsten bronzes.

In addition, a large-scale numerical study was made of the localization properties of single-particle states. In a 2D model of the band structure, the emergence of a pseudogap in the DOS was found to cause a sharp decrease in the correlation length of Fermi-level states, and thus to strongly affect the estimated position of the MIT. In a fully 3D calculation, strongly localized states — including those in the vicinity of E_F — were found to remain highly anisotropic, while states extended in a given plane decay weakly in the perpendicular direction.

A study of tantalum-substituted sodium tungsten bronzes showed that the principal effects of the additional disorder generated by the Ta sites are a greater tendency to pseudogap formation at weaker interaction strengths and a greater degree of localization of single-particle states. As for the pure sodium tungsten bronzes, interaction effects nonetheless remain dominant in determining the position of the metal-insulator transition.

ACKNOWLEDGMENTS

This research was supported by grants from the Deutsche Forschungsgemeinschaft, from the British Council, the DAAD-ARC exchange program between Great Britain and

Germany, and partially by the Fonds der Chemischen Industrie. The calculations reported here have been performed on the Siemens/Fujitsu S400 computer at the computing center in Hannover (RRZN).

APPENDIX

In order to derive the effective two- and one-band models used in Sec. IV we apply first the unitary transformations implied by Eqs. (3) and (7) to the 2D real-space three-band Ising spin UHF Hamiltonian [Eqs. (14)]. This amounts to the evaluation of its matrix elements in the basis (8) which yields the following results [cf. Eq. (10)].

(a) The diagonal elements of Eq. (10) are simply renormalized, reducing to the mean σ -spin and mean bare site energies for W and O \mathbf{k} states, respectively:

$$\langle \phi_{\mathbf{k}\sigma}^{(W)} | \hat{H} | \phi_{\mathbf{k}\sigma}^{(W)} \rangle = \frac{1}{N_{i \in W}} \sum_{i \in W} \epsilon_{i\sigma} \equiv \bar{\epsilon}_{\sigma W}, \quad (\text{A1})$$

$$\langle \phi_{\mathbf{k}\sigma}^{(1)} | \hat{H} | \phi_{\mathbf{k}\sigma}^{(1)} \rangle = \langle \phi_{\mathbf{k}\sigma}^{(2)} | \hat{H} | \phi_{\mathbf{k}\sigma}^{(2)} \rangle = \frac{1}{2N_{i \in O}} \sum_{i \in O} \epsilon_i \equiv \bar{\epsilon}_O. \quad (\text{A2})$$

In practice $\bar{\epsilon}_{\sigma W} \approx \bar{\epsilon}_{-\sigma W}$ for our finite-size system.

(b) The off-diagonal matrix elements between W and O \mathbf{k} states are entirely unaffected in the absence of disorder in the real-space hopping matrix elements (as obtains for Na_xWO_3 in our model) or

$$\langle \phi_{\mathbf{k}\sigma}^{(W)} | \hat{H} | \phi_{\mathbf{k}'\sigma'}^{(l)} \rangle = -t(\mathbf{k}) \delta_{\mathbf{k},\mathbf{k}'} \delta_{l,1} \delta_{\sigma,\sigma'}, \quad l \in \{1,2\}. \quad (\text{A3})$$

(c) Real-space diagonal disorder embodied in the effective tungsten and bare oxygen site energies introduces non-zero off-diagonal matrix elements *within* the subsets of tungsten and oxygen \mathbf{k} states, $\{\phi_{\mathbf{k}\sigma}^{(W)}\}$, $\{\phi_{\mathbf{k}-\sigma}^{(W)}\}$ and $\{\phi_{\mathbf{k}\sigma}^{(1)}, \phi_{\mathbf{k}\sigma}^{(2)}\}$, $\{\phi_{\mathbf{k}-\sigma}^{(1)}, \phi_{\mathbf{k}-\sigma}^{(2)}\}$, respectively, but none *between* these subsets [see Eq. (A3)]. The matrix elements for tungsten \mathbf{k} states are given by

$$\langle \phi_{\mathbf{k}\sigma}^{(W)} | \hat{H} | \phi_{\mathbf{k}'\sigma}^{(W)} \rangle = \frac{1}{N_{i \in W}} \sum_{i \in W} \epsilon_{i\sigma} e^{i(\mathbf{k}' - \mathbf{k}) \cdot \mathbf{r}_i}. \quad (\text{A4})$$

Since these depend only on the difference vector $\mathbf{q} = \mathbf{k}' - \mathbf{k}$, which samples the first Brillouin zone, Eq. (A4) may be written

$$\langle \phi_{\mathbf{k}\sigma}^{(W)} | \hat{H} | \phi_{(\mathbf{k}+\mathbf{q})\sigma}^{(W)} \rangle \equiv \Gamma'_\sigma(\mathbf{q}), \quad (\text{A5})$$

where

$$\Gamma'_\sigma(\mathbf{q}) = \frac{1}{N_{i \in W}} \sum_{i \in W} \epsilon_{i\sigma} e^{i\mathbf{q} \cdot \mathbf{r}_i}. \quad (\text{A6})$$

The remaining off-diagonal matrix elements between O \mathbf{k} states, $\langle \phi_{\mathbf{k}'\sigma}^{(i)} | \hat{H} | \phi_{\mathbf{k}\sigma}^{(j)} \rangle$, with $i, j \in \{1,2\}$, vanish if disorder on oxygen sites is neglected as justified in Sec. IV, which decouples a nonbonding band at the renormalized oxygen site energy $\bar{\epsilon}_O$ from the full Hamiltonian as in Eq. (10). The resultant effective two-band model for π bonding and antibonding bands is given by

$$\hat{H} = \sum_{\sigma} \hat{H}_{\sigma},$$

$$\begin{aligned} \hat{H}_{\sigma} &= \sum_{\mathbf{k}} \bar{\epsilon}_{\sigma W} \hat{n}_{\mathbf{k}\sigma}^{(W)} + \sum_{\mathbf{k}} \bar{\epsilon}_O \hat{n}_{\mathbf{k}\sigma}^{(1)} \\ &\quad - \sum_{\mathbf{k}} t(\mathbf{k}) [\hat{c}_{\mathbf{k}\sigma}^{(W)\dagger} \hat{c}_{\mathbf{k}\sigma}^{(1)} + \hat{c}_{\mathbf{k}\sigma}^{(1)\dagger} \hat{c}_{\mathbf{k}\sigma}^{(W)}] \\ &\quad + \sum_{\mathbf{k}, \mathbf{q} \neq 0} \Gamma'_\sigma(\mathbf{q}) \hat{c}_{\mathbf{k}\sigma}^{(W)\dagger} \hat{c}_{(\mathbf{k}+\mathbf{q})\sigma}^{(W)} \\ &\equiv \hat{H}_{\sigma\text{TB}}^* + \sum_{\mathbf{k}, \mathbf{q} \neq 0} \Gamma'_\sigma(\mathbf{q}) \hat{c}_{\mathbf{k}\sigma}^{(W)\dagger} \hat{c}_{(\mathbf{k}+\mathbf{q})\sigma}^{(W)}, \end{aligned} \quad (\text{A7})$$

where the fermion creation, annihilation, and number operators are defined with respect to the basis (8).

Finally, the effective two-band Hamiltonian is evaluated in the basis of renormalized CB and VB TB eigenstates of $\hat{H}_{\sigma\text{TB}}^*$ such that $\hat{H}_{\sigma\text{TB}}^*$ is diagonalized. If matrix elements between the subsets of renormalized CB and VB TB eigenstates that arise in this last unitary transformation are neglected as asserted in Sec. IV, the effective one-band model, Eq. (34), for CB states is obtained.

¹N. F. Mott, *Metal-Insulator Transitions*, 2nd ed. (Taylor & Francis, London, 1990).

²P. W. Anderson, *Phys. Rev.* **109**, 1492 (1958).

³N. F. Mott, *Philos. Mag.* **13**, 989 (1966).

⁴A. K. Raychaudhuri, K. P. Rajeev, H. Srikanth, and R. Mahendiran, *Physica B* **197**, 124 (1994).

⁵A. K. Raychaudhuri, *Adv. Phys.* **44**, 21 (1995).

⁶F. Wöhler, *Ann. Chim. Phys.* **43**, 29 (1823).

⁷P. Hagenmuller, *Prog. Solid State Chem.* **5**, 71 (1971).

⁸D. F. Holcomb, in *The Metal-Nonmetal Transition in Disordered Systems*, edited by L. R. Friedman and D. P. Tunstall (Scottish Universities Summer School in Physics, Edinburgh, 1978), p. 251.

⁹J. P. Doumerc, M. Pouchard, and P. Hagenmuller, in *The Metallic*

and Nonmetallic States of Matter, edited by P. P. Edwards and C. N. Rao (Taylor & Francis, London, 1985), p. 287.

¹⁰N. F. Mott, *Philos. Mag.* **35**, 111 (1977).

¹¹J. B. Goodenough, *Prog. Solid State Chem.* **5**, 145 (1971).

¹²M. Kielwein, K. Saiki, G. Roth, J. Fink, G. Paasch, and R. G. Egdell, *Phys. Rev. B* **51**, 10 320 (1995).

¹³M. G. Stachiotti, F. Corà, C. R. A. Catlow, and C. O. Rodriguez, *Phys. Rev. B* **55**, 7508 (1997).

¹⁴A. Hjelm, C. G. Granqvist, and J. M. Wills, *Phys. Rev. B* **54**, 2436 (1996).

¹⁵L. Kopp, B. N. Harmon, and S. H. Liu, *Solid State Commun.* **22**, 677 (1977).

¹⁶D. W. Bullet, *J. Phys. C* **16**, 2197 (1983).

¹⁷D. W. Bullet, *Solid State Commun.* **46**, 575 (1983).

- ¹⁸A. K. Raychaudhuri, Phys. Rev. B **44**, 8572 (1991).
- ¹⁹P. A. Lightsey, D. A. Lilienfeld, and D. F. Holcomb, Phys. Rev. B **14**, 4730 (1976).
- ²⁰P. P. Edwards and M. J. Sienko, Phys. Rev. B **17**, 2575 (1978).
- ²¹R. Clarke, Phys. Rev. Lett. **39**, 1550 (1977).
- ²²A. Garcia-Ruiz and Bokhimi, Physica C **204**, 79 (1992).
- ²³A. S. Ribnick, B. Post, and E. Banks, Adv. Chem. Ser. **39**, 246 (1963).
- ²⁴N. N. Garif'yanov, S. Y. Khlebnikov, I. S. Khlebnikov, and I. A. Garifullin, Czech. J. Phys. **46**, 855 (1996).
- ²⁵N. N. Garif'yanov, V. Y. Maramzin, G. Khaliullin, and I. A. Garifullin, Zh. Éksp. Teor. Fiz. **107**, 556 (1995) [JETP **80**, 301 (1995)].
- ²⁶J. P. Doumerc, P. Dordor, E. Marquestaut, M. Pouchard, and P. Hagenmuller, Philos. Mag. B **42**, 487 (1980).
- ²⁷P. Dordor, J. P. Doumerc, and G. Villeneuve, Philos. Mag. B **47**, 315 (1983).
- ²⁸M. A. Dubson and D. F. Holcomb, Phys. Rev. B **32**, 1955 (1985).
- ²⁹H. Srikanth and A. K. Raychaudhuri, J. Phys.: Condens. Matter **5**, L551 (1993).
- ³⁰A. K. Raychaudhuri, K. P. Rajeev, H. Srikanth, and N. Gayathri, Phys. Rev. B **51**, 7421 (1995).
- ³¹R. G. Egdell and M. D. Hill, Chem. Phys. Lett. **85**, 140 (1982).
- ³²M. D. Hill and R. G. Egdell, J. Phys. C **16**, 6205 (1983).
- ³³G. Hollinger, P. Pertosa, J. P. Doumerc, F. J. Himpsel, and B. Reihl, Phys. Rev. B **32**, 1987 (1985).
- ³⁴N. Tsuda, K. Nasu, A. Yanase, and K. Siratori, in *Electronic Conduction in Oxides*, Vol. 94 of *Springer Series in Solid-State Sciences*, edited by M. Cardona, P. Fulde, K. von Klitzing, and H.-J. Queisser (Springer-Verlag, Berlin, 1991).
- ³⁵B. L. Altshuler and A. G. Aronov, in *Electron-Electron Interactions in Disordered Systems*, edited by A. L. Efros and M. Pollak (North-Holland, Amsterdam, 1985).
- ³⁶J. H. Davies and J. R. Franz, Phys. Rev. Lett. **57**, 475 (1986).
- ³⁷D. P. Tunstall, Phys. Rev. B **11**, 2821 (1975).
- ³⁸B. R. Weinberger, Phys. Rev. B **17**, 566 (1978).
- ³⁹E. L. Vavilova, I. A. Garifullin, N. N. Garif'yanov, V. Y. Maramzin, G. B. Teitel'baum, and G. G. Khaliullin, Pis'ma Zh. Éksp. Teor. Fiz. **58**, 625 (1993) [JETP Lett. **58**, 625 (1993)].
- ⁴⁰W. A. Kamitakahara, B. N. Harmon, J. G. Taylor, L. Kopp, H. R. Shanks, and J. Rath, Phys. Rev. Lett. **36**, 1393 (1976).
- ⁴¹T. Akahane, K. R. Hoffmann, T. Chiba, and S. Berko, Solid State Commun. **54**, 823 (1985).
- ⁴²R. L. Benbow, M. R. Thuler, and Z. Hurych, Phys. Rev. B **25**, 7097 (1982).
- ⁴³T. Wolfram, Phys. Rev. Lett. **29**, 1383 (1972).
- ⁴⁴R. Salchov, R. Liebmann, and J. Appel, J. Phys. Chem. Solids **44**, 245 (1983).
- ⁴⁵T. Wolfram and L. Sutcu, Phys. Rev. B **31**, 7680 (1985).
- ⁴⁶T. Koslowski and W. von Niessen, Philos. Mag. B **67**, 317 (1993).
- ⁴⁷W. A. Harrison, *Electronic Structure and the Properties of Solids* (Freeman, San Francisco, 1980).
- ⁴⁸V. J. Emery, Phys. Rev. Lett. **58**, 2794 (1987).
- ⁴⁹P. Fulde, in *Electron Correlations in Molecules and Solids*, Vol. 100 of *Springer Series in Solid State Sciences*, edited by M. Cardona, P. Fulde, K. von Klitzing, and H.-J. Queisser (Springer-Verlag, Berlin, 1991).
- ⁵⁰E. Dagotto, Rev. Mod. Phys. **66**, 763 (1994).
- ⁵¹C. Dasgupta and J. W. Halley, Phys. Rev. B **47**, 1126 (1993).
- ⁵²M. A. Tusch and D. E. Logan, Phys. Rev. B **48**, 14 843 (1993).
- ⁵³C. Lanczos, J. Res. Natl. Bur. Stand. Sect. B **45**, 225 (1950).
- ⁵⁴J. K. Cullum and R. Willoughby, *Lanczos Algorithms for Large Symmetric Eigenvalue Problems* (Birkhäuser, Boston, 1985), Vol. I.
- ⁵⁵J. K. Cullum and R. Willoughby, *Lanczos Algorithms for Large Symmetric Eigenvalue Problems* (Birkhäuser, Boston, 1985), Vol. II.
- ⁵⁶T. Koslowski and W. von Niessen, J. Comput. Chem. **14**, 769 (1993).
- ⁵⁷P. Dean, Rev. Mod. Phys. **44**, 127 (1972).
- ⁵⁸H. R. Schwarz, *Methode der Finiten Elemente, Teubner Studienbücher*, 3rd ed. (B. G. Teubner, Stuttgart, 1991).
- ⁵⁹T.-M. Chang, J. D. Bauer, and J. L. Skinner, J. Chem. Phys. **93**, 8973 (1990).
- ⁶⁰M. P. Allen and D. J. Tildesley, *Computer Simulation of Liquids* (Oxford University Press, Oxford, 1987).
- ⁶¹R. J. Bell and P. Dean, Discuss. Faraday Soc. **50**, 55 (1970).
- ⁶²Q. Li, C. M. Soukoulis, E. N. Economou, and G. S. Grest, Phys. Rev. B **40**, 2825 (1989).
- ⁶³D. E. Logan and F. Siringo, J. Phys.: Condens. Matter **5**, 1841 (1993).
- ⁶⁴M. A. Dubson and D. F. Holcomb, Phys. Rev. B **34**, 25 (1986).
- ⁶⁵B. S. Shastry, Phys. Rev. Lett. **63**, 1288 (1989).
- ⁶⁶T. Wolfram and S. Ellialtıođlu, Phys. Rev. B **25**, 2697 (1982).
- ⁶⁷J. Zhong and H.-B. Schüttler, Phys. Rev. Lett. **69**, 1600 (1992).
- ⁶⁸R. G. Egdell and G. B. Jones, J. Solid State Chem. **81**, 137 (1991).
- ⁶⁹D. P. Tunstall and W. Ramage, J. Phys. C **13**, 725 (1980).
- ⁷⁰I. A. Garifullin, N. N. Garif'yanov, V. Y. Maramzin, and G. G. Khaliullin, Pis'ma Zh. Éksp. Teor. Fiz. **54**, 380 (1991) [JETP Lett. **54**, 375 (1991)].
- ⁷¹I. A. Garifullin, N. N. Garif'yanov, V. Y. Maramzin, and G. G. Khaliullin, Solid State Commun. **85**, 1001 (1993).